



**Pedro Miguel Gaspar
Novais**

**Development and optimization of an aerodynamic
device for the UA Formula Student car**

Desenvolvimento e otimização de um dispositivo
aerodinâmico para o carro do Formula Student UA



**Pedro Miguel Gaspar
Novais**

**Development and optimization of an aerodynamic
device for the UA Formula Student car**

Desenvolvimento e otimização de um dispositivo
aerodinâmico para o carro do Formula Student UA

Dissertação apresentada à Universidade de Aveiro para cumprimento dos requisitos necessários à obtenção do grau de Mestre em Engenharia Mecânica, realizada sob orientação científica de Vítor António Ferreira da Costa, Professor Catedrático, Departamento de Engenharia Mecânica, Universidade de Aveiro.

o júri / the jury

presidente / president

Prof. Doutor João Alexandre Dias de Oliveira

Professor Auxiliar da Universidade de Aveiro

Prof. Doutor António Manuel Gameiro Lopes

Professor Auxiliar do Departamento de Engenharia Mecânica da Faculdade de Ciências e Tecnologia, Universidade de Coimbra

Prof. Doutor Vítor António Ferreira da Costa

Professor Catedrático da Universidade de Aveiro (orientador)

**agradecimentos /
acknowledgements**

Gostaria de expressar o meu agradecimento aos vários professores que surgiram ao longo de toda a minha formação, por todos os ensinamentos que me foram transmitidos. Em especial ao Professor Doutor João Oliveira pelas sugestões feitas relativas ao processo de otimização presente neste trabalho.

Gostaria também de endereçar os meus sinceros agradecimentos ao meu orientador, o Professor Doutor Vítor Costa, por ter investido parte do seu precioso tempo para me dar apoio, pelo rigor exigido e pelas suas valiosas e construtivas sugestões.

Uma palavra de apreço também a todos os colegas que me acompanharam durante este processo e pelas experiências e conhecimento que partilharam.

Em último lugar, estou imensamente grato á minha família, em especial aos meus pais por todo o apoio dado e motivação em seguir os meus sonhos independentemente de tudo o resto.

Esta Dissertação teve o apoio dos projetos: UIDB/00481/2020 and UIDP/00481/2020 - Fundação para a Ciência e a Tecnologia; and CENTRO-01-0145-FEDER-022083 - Centro Portugal Regional Operational Programme (Centro2020), under the PORTUGAL 2020 Partnership Agreement, through the European Regional Development Fund.

keywords

Formula Student, CFD, Harmony Search Algorithm, Car rear wing, Optimization

abstract

The development and optimization of the rear wing of a Formula Student car must be done with the aid of CFD numerical simulations, since in order to ensure a good aerodynamic performance a great number of wing configurations need to be tested. The aim of this thesis was to develop a fully functional optimization code, that could be easily adapted to generate the optimal rear wing for any given Formula Student car, only needing the car CFD results. As a means to accomplish that, a CFD simulation was performed to the Formula Student Aveiro teams' car and additional wind tunnel testing was conducted with the purpose of corroborating the simulation results. Hereupon, the velocity profile at the car rear end, obtained in the CFD simulation, was used as the inlet in the rear wing simulation for the optimization process, allowing a contribution of the car geometry to the rear wing optimization without the addition of unnecessary computational time. Finally, an optimization code based on the Harmony Search Algorithm was created to define the optimal rear wing parameters and with that achieve an optimized rear wing configuration. The optimized configuration consists of 4 airfoils, and showed excellent results even surpassing the rear wing performance of the 2016 FSAE Czech Republic competition winner.

palavras-chave

Formula Student, CFD, Harmony Search Algorithm, Asa traseira, Otimização

resumo

O desenvolvimento e otimização da asa traseira de um carro do tipo Formula Student devem ser tratados através de simulações numéricas do tipo CFD, dado que, para assegurar uma boa performance aerodinâmica da asa traseira, teriam de ser testados um grande número de configurações. O objetivo deste trabalho era desenvolver um código de otimização completamente funcional, capaz de ser facilmente adaptado, de forma a gerar uma asa traseira ótima para qualquer veículo do tipo Formula Student, sendo apenas necessários os resultados da simulação CFD. De forma a cumprir o proposto, foi realizada ao carro da equipa de Formula Student da UA uma análise CFD, tendo, adicionalmente, sido efetuados testes no túnel de vento com o propósito de corroborar os resultados da simulação. Tendo em consideração o exposto, o perfil de velocidades na parte traseira do carro, obtido através da sua simulação CFD, foi usado como Inlet na simulação da asa traseira para o processo de otimização, permitindo a contribuição da geometria do carro para o processo de otimização da asa traseira sem a adição de tempo computacional desnecessário. Por fim, foi criado um código de otimização baseado no Harmony Search Algorithm, com o propósito de otimizar os parâmetros que definem a geometria da asa traseira e com isso obter com uma configuração otimizada. A configuração otimizada é composta por 4 airfoils, tendo demonstrado excelentes resultados, ultrapassando até o desempenho da asa traseira da equipa que ganhou a competição FSAE Czech Republic, em 2016.

Contents

I	Introduction and Background	1
1	Introduction	3
1.1	Thesis Objectives	3
1.2	Thesis Outline	3
2	Automotive aerodynamics and FSAE competition	5
2.1	FSAE competition history	5
2.2	Impact of aerodynamics on FSAE cars	5
2.2.1	Front wing	6
2.2.2	Undertray diffuser	7
2.2.3	Rear wing	7
2.3	FSAE rear wing rules/constraints	10
2.4	Methods to evaluate aerodynamic performance	11
II	Process and Results	13
3	CFD theoretical background	15
3.1	Fundamental Equations	15
3.2	Finite Volume Method	19
3.3	Computing Forces	20
3.4	Boundary layer	21
3.5	Turbulence models	23
4	Car CFD simulation process	25
4.1	Model preparation	25
4.2	Meshing	27
4.2.1	Surface mesh	27
4.2.2	Volume mesh	30
4.3	Setup and boundaries	32
4.3.1	Turbulence model	33
4.3.2	Boundary conditions and reference values	33
4.3.3	Solution methods and controls	34
4.4	Results and post-processing	35
4.4.1	y^+ value and boundary layer definition	35

4.4.2	Mesh independence studies	37
4.4.3	CFD results	38
5	Wind tunnel experiments	41
5.1	Wind tunnel specifications and car model	41
5.2	Flow visualization techniques	43
5.3	CFD results vs wind tunnel measurements	45
6	Rear wing optimization	47
6.1	Problem definition	47
6.2	Formulation and problem classification	51
6.3	Evaluation process	54
6.3.1	Geometry generation	55
6.3.2	Pre-processing	56
6.3.3	Meshing/Solving	59
6.3.4	Optimization algorithm	65
6.4	Optimization improvement runs	68
6.4.1	Test run with $S_1 = C_l$	68
6.4.2	Test run with $S_1 = Lift$	70
6.4.3	Test run with low quality mesh	72
6.4.4	Test run for one rear wing combination type	73
6.5	Final results	73
III	Conclusions and suggestions for future work	77
7	Conclusions and suggestions for future work	79
	Bibliography	80

List of Tables

4.1	Boundary Conditions.	33
4.2	Fluid flow reference values.	34
4.3	Spatial discretization schemes selected for the numerical analyses in ANSYS Fluent while using the Spalart-Allmaras turbulence model.	34
4.4	Spatial discretization schemes selected for the numerical analyses in ANSYS Fluent while using the SST $k - \omega$ turbulence model.	35
6.1	Boundary conditions.	60
6.2	Fluid flow reference values.	63

Intentionally blank page.

List of Figures

2.1	CAD of the team’s car before construction.	6
2.2	Car under construction.	6
2.3	Typical FSAE car front wing [4].	7
2.4	Typical FSAE car undertray diffuser [4].	8
2.5	Typical FSAE car rear wing [4].	9
2.6	How rear wing end-plates reduce drag and improve the aerodynamic efficiency [4].	9
2.7	Representation of positioning restrictions [2].	10
3.1	Finite control volume fixed in space [12].	16
3.2	Typical polygonal 2D cell.	19
3.3	Boundary layer around an airfoil [12].	21
3.4	Boundary layer regions[12].	21
3.5	Velocity profile for a reversed flow [12].	21
3.6	Boundary layer subdivisions [17].	23
4.1	Car CAD model.	25
4.2	Enclosure and body of influence.	26
4.3	Wheel/ground interaction.	26
4.4	First iteration of the Car surface mesh (lateral view).	27
4.5	BOI consideration in the car and enclosure surface mesh.	28
4.6	Wheel and suspension rods surface mesh refinement.	28
4.7	Firewall and chassis surface mesh refinement.	29
4.8	Volume mesh section view.	30
4.9	Volume mesh transition layers.	31
4.10	Volume mesh section view boundary layer poly-prims.	32
4.11	Number of cells vs skewness.	32
4.12	Frontal area of half of the car.	34
4.13	Scheme of the y^+ iterative process.	36
4.14	Symmetry plane contour of the turbulence viscosity ratio.	37
4.15	C_l and C_d values for tested meshes.	38
4.16	Pathlines along the car geometry plane views.	38
4.17	Velocity contours on the car symmetry plane and near the rear wing placement region.	39
4.18	Pathlines along the car geometry.	39
5.1	Wind tunnel used for the experiments	41
5.2	Scaled model of the car.	43

5.3	Trip moulding technique [23].	43
5.4	PIV used setup system [24].	44
5.5	PIV section planes.	44
5.6	Velocity vector field for plane 1 for both wind tunnel(left) and CFD(right).	45
5.7	Velocity vector field for plane 2 for both wind tunnel(left) and CFD(right).	46
6.1	Top view of the general rear wing within the competition rules.	48
6.2	Side view of the general rear wing within the competition rules.	48
6.3	Airfoil configurations used in the optimization.	49
6.4	Variables that control the relative positioning of the airfoils.	50
6.5	Variables that control the shape of the airfoils.	50
6.6	Airfoil configurations and relative organization.	53
6.7	Diagram of the evaluation process.	54
6.8	NACA 4 series shape functions (http://airfoiltools.com/airfoil/naca4digit).	55
6.9	Open trailing edge representation of a created geometry.	55
6.10	Transition from the generated geometry to pre-processing.	56
6.11	3D rear wing with its end-plate.	57
6.12	Simulation enclosure and body of influence	57
6.13	Named selections created for the mesh refinement.	58
6.14	Transition from the generated geometry to pre-processing.	58
6.15	Surface mesh for one of the generated wing geometries.	59
6.16	Volume mesh for one of the generated wing geometries.	60
6.17	New car enclosure for the rear wing inlet velocity profile values.	61
6.18	Plane for the capture of the inlet velocity profile values.	61
6.19	Velocity profiles captured from the plane created for the car simulation.	62
6.20	Velocity profiles from the rear wing inlet after a simulation.	62
6.21	C_l , C_d and run time of the simulations for the different tested meshes.	64
6.22	Transition from the simulation to the optimization code.	64
6.23	HSA flowchart.	66
6.24	Harmony memory structure of the HSA [32].	67
6.25	HM evolution and wing shapes with high levels of performance for each type of configuration for test run 1.	69
6.26	HM values at the end of the first test run.	70
6.27	<i>Lift</i> and C_l best values during the evaluation process.	70
6.28	HM evolution and wing shapes with high levels of performance for each type of configuration for test run 2.	71
6.29	HM values at the end of the second test run.	71
6.30	HM evolution and wing shapes with high levels of performance for each type of configuration for test run 3.	72
6.31	HM values at the end of the third test run.	73
6.32	HM evolution and wing shapes with high levels of performance for each type of configuration for test run 4.	74
6.33	HM values at the end of the fourth test run.	74
6.34	HM evolution and wing shapes with high levels of performance for each type of configuration for the final run.	75
6.35	HM values at the end of the final run.	76
6.36	Optimized rear wing.	76

List of Symbols

The following list describes several symbols that will later be used within the body of the document:

μ	Dynamic viscosity of the fluid
ν	Kinematic viscosity of the fluid
ρ	Density of fluid
τ	Shear stress
bw	Bandwidth
C	Courant number
C_d	Drag coefficient
C_l	Lift coefficient
D	Drag force
f	Net body force per unit mass
F	Force exerted on the fluid
$F_{Viscous}$	Viscous force
$HMCR$	Harmony memory considering rate
L	Lift force
m	Mass
M	Point of maximum camber
p	Pressure

P	Airfoil maximum camber
PAR	Pitch adjusting rate
Re	Reynolds number
Re_{cr}	Critical Reynolds number
t	Time
T	Airfoil maximum thickness
\bar{u}_i	Mean velocity components
u'_i	Fluctuating velocity components
u_t	Friction velocity
U^+	Dimensionless velocity
V	Velocity
V_{in}	Inlet flow velocity
x_{cr}	Position of the transition to turbulent flow
y_p	Distance from the centroid of the wall-adjacent cell to the wall
y^+	Dimensionless normal distance from the surface

Part I

Introduction and Background

Chapter 1

Introduction

1.1 Thesis Objectives

The aim of this thesis is to develop a fully functional optimization code, that can be easily adapted to generate the optimal rear wing for any given Formula Student car, only needing the car CFD results. As means to accomplish that, CFD simulations were performed to the Formula Student Aveiro teams' car and an optimization code based on the Harmony Search Algorithm was created. Throughout this thesis all the development process of both the Formula Student car simulation and the optimization process will be described in detail.

1.2 Thesis Outline

The present thesis document is organised as follows:

- In Chapter 2, a brief literature review on the aerodynamics of FSAE cars is made, as well as the introduction of mainly conventional aerodynamic devices concepts, its influence on the vehicle performance and the methods used to evaluate vehicles' aerodynamic performance and behaviour.
- In Chapter 3, a broad overview of the aerodynamics fundamental equations is given and a description on how CFD software approximately solves them.
- In Chapter 4 it is possible to find a description of the simulation process of the car model, working as starting point for the rear wing optimization.
- In Chapter 5, a description of the wind tunnel testing and the car scaled model setup is made, as well as the used fluid flow visualization techniques.
- In Chapter 6, the rear wing optimization development process is described, and the optimization process is submitted to a number of tests resulting on the optimized rear wing.
- Lastly, there is a brief extension on the conclusions of this work, as well as suggestions for future work.

Intentionally blank page.

Chapter 2

Automotive aerodynamics and FSAE competition

2.1 FSAE competition history

Founded in 1981 by Dr. Ronald Matthews at The University of Texas at Austin, the Formula SAE collegiate design series is the largest intercollegiate design competition in the World. Every year, Formula SAE teams at universities around the World design, build, and race a single-seater, open wheel formula-style car.[1]

Formula Student is the European version of the American Formula SAE competition, whose main purpose is to produce a race car prototype which will be competing against cars from different teams. "Teams are to assume that they work for an engineering firm that is designing, fabricating, testing and demonstrating a prototype vehicle", and the vehicle should be high performant. In addition to vehicle performance, there are other design factors as "aesthetics, cost, ergonomics, maintainability and manufacturability", that will be judged to determine the best overall car in terms of cost, reliability and performance.[2]

Teams initially go through an extensive and thorough evaluation of the car, to verify if every single component has been built accordingly to the competition regulations. This being followed by dynamic events, in which the cars performance is tested in different scenarios such as acceleration, autocross and endurance.

The car under analysis in this thesis, belongs to the UA Formula Student team, whose development involves 30-40 students each year. The team was founded in 2006 and it is now building its first internal combustion engine car, Figures ?? 2.2.

2.2 Impact of aerodynamics on FSAE cars

Air resistance is the major obstacle to automotive speed and fuel saving since the dawn of the automobile. There was nothing aerodynamic about the earliest cars, but with the first races between constructors, fast circuits with low power engines made engineers realise how much the aerodynamic drag force increases significantly with the vehicle speed.[3] Hereupon, nowadays aerodynamic performance has a major role within the racing scene, having the purpose of increasing the normal load on the tires/ground interaction, for increased grip, without the corresponding addition of mass. The cor-

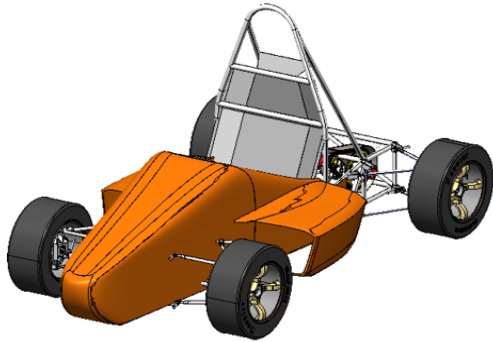


Figure 2.1: CAD of the team's car before construction.



Figure 2.2: Car under construction.

nering quality of a car is greatly influenced by the amount of grip available in the tires, along with aerodynamic drag and engine power, setting the theoretical limits for the vehicle's velocity around the track. Meaning that the main objective of an aerodynamic package is to increase the cars downforce, the aerodynamic load that will be applied perpendicularly to the tires/ground interaction, while decreasing drag ,(the horizontal force that opposes the car movement).

Aerodynamic upgrades are one of the key areas in a FSAE car development, which can easily make a difference in competition events, with direct effect on the top and cornering speed. Depending on the required goals of every team, they can either choose to reduce drag and increase top speed, or increase down force and drag levels for cornering speeds, or even aim for a balance between the two. In order to obtain the intended results in competitions, three diverse aerodynamic devices are commonly used in FSAE cars.

2.2.1 Front wing

The front wing, Figure 2.3, is designed with the purpose of setting up the airflow for the entire vehicle while producing downforce. Operating in ground effect due to its proximity to the road and typically having a multi-element design.[Katz2006]

Since the front wing is the first object to disturb flow around the vehicle, a poorly designed front wing can result in very large drag increases and losses across the entire rear of the car. Front wings are normally mounted close to the suspension, or even on the mounts in order to transmit downward loads as effectively as possible and create downforce, usually being responsible for about 20% - 30% of the total downforce on the car.

"The interaction between the front wheels and the front wing makes it very difficult to come up with the best solution;however, most teams are using a front wing in order to deflect the oncoming air around the front tires" [4]. The exposed wheels of a FSAE

car probably induce more drag than any other part of the car. Since the FSAE rules prohibit any cover of the wheels, an inevitable large separation of the flow takes place and this causing large amounts of drag.



Figure 2.3: Typical FSAE car front wing [4].

2.2.2 Undertray diffuser

The undertray, Figure 2.4, seeks to utilize the underbody of the car to produce downforce. Similar to the front wing it also operates in ground effect, where the Venturi effect is applied allowing a low pressure area beneath the bodywork. By shaping the underbody as an inverted wing, or with appropriate tunnels, the pressure between the undertray and the ground decreases, thus creating additional downforce.

The undertray is not only the largest aerodynamic component on a FSAE car, it's also the most aerodynamically efficient, producing nearly 9 times more downforce per unit of drag force than a rear wing due to its wetted area underneath the car. Properly designed diffusers are the most efficient at generating downforce, while keeping the drag force relatively low.

The diffuser, Figure 2.3, is the rear element at the underbody of a FSAE car close to the floor. This is the last component where air interacts with the car. The objective of the diffuser is to slow the flow down and to give the used air flow from the undertray of the car as much possible space to exit from the rear end. This ultimately means that if the air can escape more easily from under the car, then more air at faster velocities can flow under the undertray of the car creating a lower pressure and therefore higher downforce.[4]

2.2.3 Rear wing

The rear wing, Figure 2.5, is a crucial component for the performance of a FSAE car. This device contributes to approximately 30 % of the car's total downforce. The main function of the rear wing is to help primarily in braking and cornering forces for the rear tires and with that eliminate over steering.

The rear wing is a multi-element airfoil, usually comprised of three or four sets of elements connected to each other by the wing end-plates. Multiple slats and flaps are used to gain more downforce in the rear wing. The lift coefficient increases and

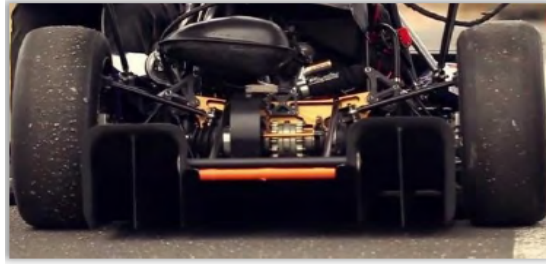


Figure 2.4: Typical FSAE car undertray diffuser [4].

lift/drag ratio decreases when increasing the number of airfoils. Usually the main wing produces the most amount of downforce and the remaining elements have the purpose of delaying flow separation and improve the main wing efficiency while still producing a considerable amount of downforce. The airfoil shape is usually based on the NACA airfoil data base, and the same shape is used for all elements. [4, 5, 6, 7, 8]

The airflow at the rear of the car can be affected by many different influences from the rest of the car and so it is called "dirty", because the flow that the rear wing will be subjected to is mainly a separated flow with a lot of turbulence. This causes the rear wing to be less aerodynamically efficient than the front wing, due to the disbursed airflow that is not ideal. Since the travel speeds during competition are relatively low, reaching a maximum of around 120 km/h, and the air that reaches the rear wings is "dirty", they have a considerable size when comparing to other aerodynamic devices in order to produce the desirable aerodynamic forces.

However, the rear wing typically generates the double of the downforce generated by the front wing so that the handling balance of the car is maintained, but this also depends on the design and the suspension set up of each FSAE car. A greater rear wing angle increases the downforce and produces more drag, therefore reducing the cars top speed. So, when racing on FSAE tracks with long straights and few turns it is better to design the rear wings to have small angles of attack. On the contrary, when the car is racing on FSAE tracks with many turns and few straights, more downforce is beneficial thus it is better to design the wings to have greater angles of attack.

Rear wing end-plates, Figure 2.6, are designed with a purpose in mind. Due to their form, they provide a convenient way of mounting wings. However, the main purpose and aerodynamic function of these end-plates is to prevent air spillage around the wing tips and thus delay the development of trailing vortices. Trailing vortex or induced drag is the dominating drag on any kind of wings, having more impact in low aspect ratio wings. An additional function of the rear end-plates is to help reduce the influence of up flow from the wheels. With the use of end-plates, vortices will develop later on the wing, because the airflow is forced to move in one direction and can only start mixing with disrupted air flow inside the wing after the end-plate ends.

All these aerodynamic devices have to be developed in harmony to allow an aerodynamically balanced car, since each one of these components is located in distinct zones of the car creating a moment about its center of mass. The rear wing is often the last one to be designed and used to balance the car after the front wing setup has been completed to compensate for any possible undesirable handling characteristics of the car.



Figure 2.5: Typical FSAE car rear wing [4].

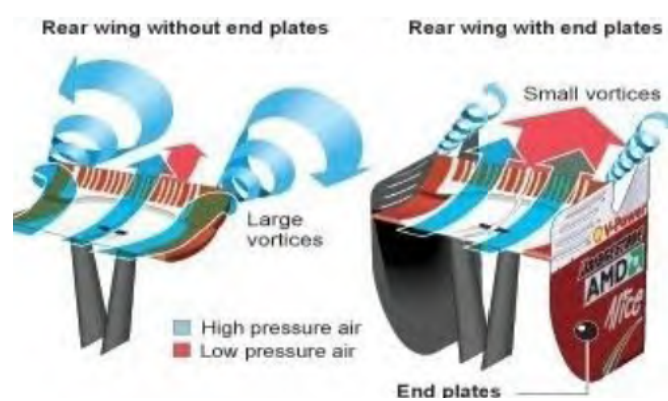


Figure 2.6: How rear wing end-plates reduce drag and improve the aerodynamic efficiency [4].

2.3 FSAE rear wing rules/constraints

The following rules are imposed by the FSAE competition and function as restrictions along the development of aerodynamic devices, working both as security and performance control. Below are excerpts from the regulations that apply to the rear wing and other aerodynamic devices and representation of the positioning restrictions, Figure 2.7.[2]

T.7.1.4	All forward facing edges that could contact a pedestrian (wings, end plates, and undertrays) must have a minimum radius of 5 mm for all horizontal edges and 3 mm for vertical edges. This may be the radius of the edges themselves, or additional permanently attached pieces designed to meet this requirement.
T.7.1.5	Other edges that a person may touch must not be sharp
T.7.4	Length
	In plan view, any part of any Aerodynamic Device must be:
a.	No more than 700 mm forward of the fronts of the front tires
b.	No more than 250 mm rearward of the rear of the rear tires
T.7.5.3	When rearward of the Head Restraint Plane : Inboard of two vertical planes parallel to the centerline of the chassis touching the inside of the rear tires at the height of the hub centerline.
T.7.6	Height
T.7.6.1	Any part of any Aerodynamic Device that is located:
a.	Rearward of the Head Restraint Plane must be no higher than 1200 mm above the ground.

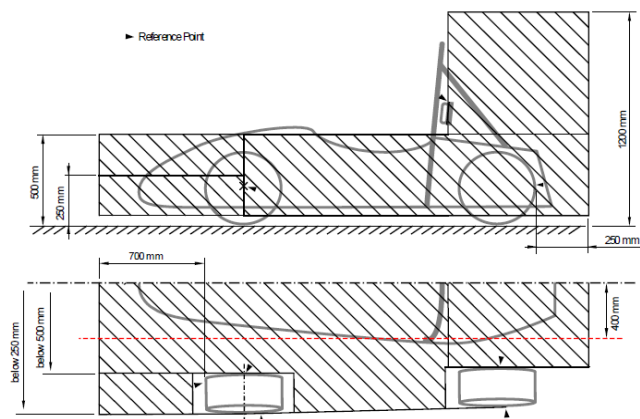


Figure 2.7: Representation of positioning restrictions [2].

2.4 Methods to evaluate aerodynamic performance

As one of the major sources of energy losses in road vehicles, aerodynamic forces play an important role on their performance and have been a major point of interest for the racing industry in the last decades. During that time, some aerodynamic performance evaluating tools were developed; wind tunnel experiments, on-road experiments, and Computational Fluid Dynamics (CFD) modeling can be listed as the three most common ones.[9] However, on-road experiments cannot be used as a development tool, since a completed car must be manufactured for such assessment; as a result, CFD simulations and wind tunnel experiments are kept as the tools that allow an aerodynamic performance evaluation. Both CFD analysis and wind tunnel experiments have their limitations when it comes to fully reproducing the actual on-road aerodynamic performance of the vehicle. For wind tunnels, usually scaled models are used which, especially for smaller scales, can increase the risks regarding the results' transfer to full scale.[10] For example, the ratio of solid blockage in wind tunnels can interfere with the results and impose a limitation on the size of the model and, in some cases, it could be difficult to follow Reynolds law of similarity since wind tunnels have a limited top speed. When it comes to CFD analyses, even though CFD capabilities have greatly been improved with the rapid growth of computational power, showing a much better correlation with wind tunnel measurements, they will always be a representation of reality. [11] Although these two different approaches are not able to fully replicate the on-road aerodynamic performance, they can reach a great level of accuracy and entail much lower costs when compared with on-road experiments, especially in the case of CFD analysis.[9]

In the design of a FSAE race car, one is challenged with numerous instances of complex geometries, rotating wheels, sidepods, the driver among many others. The nature of these vehicles makes it almost impossible to approach the problem of aerodynamic optimization of the entire car analytically or only using wind tunnel testing. It is due to these obstacles that simulation methods, as CFD are the main focus while developing an aerodynamic package.

In this thesis the CFD method was adopted, ANSYS fluent R19 being the chosen CFD interface, complemented with wind tunnel testing with the purpose of corroborating qualitative results of flow streamlines in specific locations of the model. The CFD simulations were also complemented with wind tunnel testing, in which was possible to observe flow phenomena around the car and compare them with the CFD results, which will be described with more detail in Chapter 5.

Intentionally blank page.

Part II

Process and Results

Chapter 3

CFD theoretical background

As referred in Section 2.4, an analytical analyses wouldn't be viable due to the complexity of the problem under analysis. So, CFD was used to simulate the car aerodynamics. In this chapter a broad overview of the aerodynamics fundamental equations is given, and a description on how CFD software works them.

For the following sub-chapters (3.1) and (3.2), two books were closely followed and taken as reference, Chapter 2 from John D.Anderson (2013) [12] and Chapter 4 from Ferziger and Peric (2002) [13] correspondingly.

3.1 Fundamental Equations

CFD is defined as “the art of replacing the integrals or the partial derivatives (as the case may be) in these equations with discretized algebraic forms, which in turn are solved to obtain numbers for the flow field values at discrete points in time and/or space.”[14]

As most of partial differential equations don't have any analytical solutions, only approximate results can be achieved through iterative processes. That is possible by invoking three fundamental physical principles that are deeply ingrained in our macroscopic observations of Nature, namely,[12]

- Mass is conserved , meaning that mass can be neither created nor destroyed.
- Newton's second law: force = momentum time rate of change.
- Energy is conserved; it can only change from one form to another or, be exchanged between different bodies/systems.

Through an analysis of these physical principles, it is possible to derive three equations which are able to mathematically represent a real, time dependent, three-dimensional fluid flow around a body. Those are the continuity equation (mass conservation), momentum equations (momentum conservation) and energy balance equation (energy conservation).

Continuity equation

Adopting the physical principle that no mass can be neither created or destroyed, and applying that same concept to a finite control volume fixed in space, as shown in Figure

3.1.

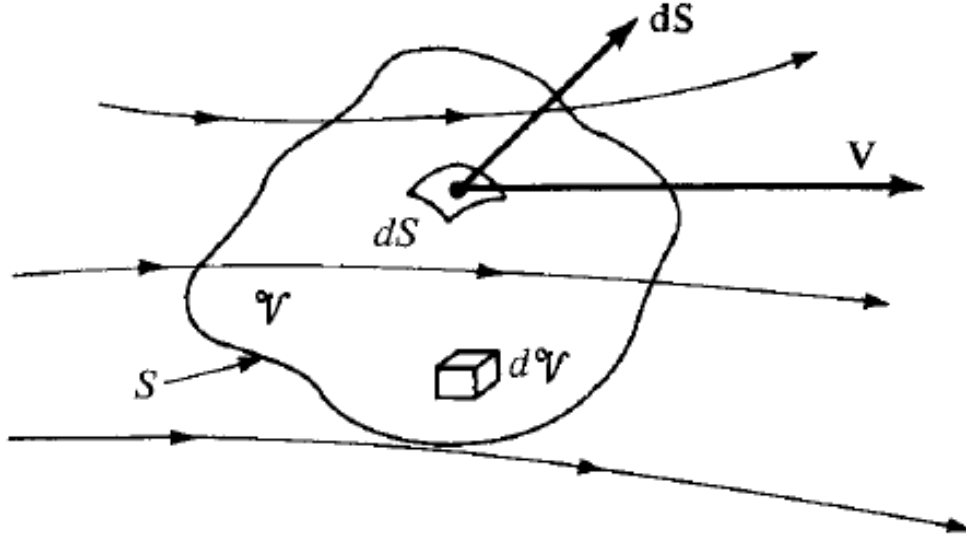


Figure 3.1: Finite control volume fixed in space [12].

It can be inferred that the net mass flow out of control volume through its surface S is equal to the time rate of decrease of mass inside the control volume v , which can be formulated as,

$$\oiint_S \rho \mathbf{V} \cdot d\mathbf{S} = -\frac{\partial}{\partial t} \iiint_v \rho dv \quad (3.1)$$

where \mathbf{V} is the velocity vector, and the product $\rho \mathbf{V}$ represents the mass flux through a superficial area perpendicular to \mathbf{V} . The vector representing that same elemental surface area is $d\mathbf{S}$. Also dv is an elemental volume inside the control volume.

Examining Equation (3.1) it is known, by convention, that $d\mathbf{S}$ always points in an outwards direction of the control volume [12]. Meaning that if \mathbf{V} is pointing out of the control volume, then mass is leaving (outflow) and the product $\mathbf{V} \cdot d\mathbf{S}$ is positive; on the contrary, if \mathbf{V} is pointing into the control volume then mass is entering the control volume (inflow) and the product $\mathbf{V} \cdot d\mathbf{S}$ is negative. This to conclude, that a negative sign is needed on the right term of Equation (3.1) so that a negative time rate of mass inside the control volume v coincides with an outflow through S .

By applying the divergence theorem to the left side of Equation 3.1 and placing the time derivative inside the volume integral, what is possible since the control volume is fixed in space thus so the limits of integration, Equation (3.2) is obtained,

$$\iiint_v \left[\frac{\partial \rho}{\partial t} + \nabla \cdot (\rho \mathbf{V}) \right] dv = 0 \quad (3.2)$$

Examining Equation (3.2) there are two different ways that the integral would be equal to zero. The first option is if the integrand part was a finite number, since in that case the integral over part of the control volume would have to be identical in magnitude and opposite in sign. "However, the finite control volume is arbitrarily drawn in space;

there is no reason to expect cancellation of one region by the other.”[12]. From this assumption it is possible to conclude that the only way that the integral may be zero is if the integrand is zero at all points of the control volume, thus reaching the following equation

$$\frac{\partial \rho}{\partial t} + \nabla \cdot (\rho \mathbf{V}) = 0 \quad (3.3)$$

Momentum equations

Adopting the physical principle that the sum of all forces applied to a body are equal to the time rate of momentum change, Newton’s second law of motion and with a constant mass it is possible to deduce the following equation

$$\mathbf{F} = \frac{\partial}{\partial t}(m\mathbf{V}) \quad (3.4)$$

where \mathbf{F} is the force exerted on the fluid as it flows through the control volume [12]. Using the model of a finite control volume, present in Figure 3.1, there are two types of forces that can act on the fluid inside v , being these, body forces as gravity and surface forces, as shear stress. The forces exerted on the fluid can be formulated as follows

$$\mathbf{F} = - \iint_S p \, dS + \iiint_v \rho \mathbf{f} \, dv + \mathbf{F}_{Viscous} \quad (3.5)$$

where the closed surface integral of pressure p represents the pressure applied by the surroundings to the fluid, being negative for an inward pressure, since it has the opposite direction of $d\mathbf{S}$. The force \mathbf{f} represents the net body force per unit mass, which can be defined by the force per unit mass exerted on the fluid, and finally $\mathbf{F}_{Viscous}$ is the total viscous force applied to the control surface.

A change in momentum inside v , caused by an external force implicitly means that the momentum existent inside the control volume, at a certain instant, plus the variation of momentum through the delimiting surface S (outflow minus the inflow of momentum) has to equal that same external force, which can be equated as follows

$$\frac{\partial}{\partial t}(m\mathbf{V}) = \frac{\partial}{\partial t} \iiint_v \rho \mathbf{V} \, dv + \iint_S (\rho \mathbf{V} \, dS) \mathbf{V} \quad (3.6)$$

where the closed volume integral represents the time rate of change of momentum contained inside the control volume for an unsteady/transient flow. The closed surface integral represents the variation of momentum through the delimiting surface S similar to what was applied in Equation (3.1), but now multiplied by the flow velocity.

Replacing both Equation (3.5) and (3.6) in equation (3.4) it is possible to obtain the full momentum equation in its integral form, equated as follows

$$- \iint_S p \, dS + \iiint_v \rho \mathbf{f} \, dv + \mathbf{F}_{Viscous} = \frac{\partial}{\partial t} \iiint_v \rho \mathbf{V} \, dv + \iint_S (\rho \mathbf{V} \, dS) \mathbf{V} \quad (3.7)$$

Through a similar process to the one used to obtain Equations (3.2) and (3.3), applying both the divergence theorem and the assumptions made in [12] to Equation (3.7), it

is possible to achieve the Navier-Stokes equations in its vector form

$$\frac{\partial \rho \mathbf{V}}{\partial t} + \nabla \cdot (\rho \mathbf{V}) \mathbf{V} = -\nabla p + \rho \mathbf{f} + \mathbf{F}_{Viscous} \quad (3.8)$$

Incompressible steady flow assumptions

For the scope of this thesis, and the simulation of both car and rear wing, the following assumptions/simplifications can be made:

- Fully developed (steady-state) flow ($\frac{\partial}{\partial t} \equiv 0$)
- Negligible gravitational force ($\mathbf{f} = 0$)
- Incompressible flow ($\rho = \text{constant}$)

Although a CFD transient flow analysis is possible and would be within this thesis subject, it would increase the complexity of the process and for now a steady state simulation revealed to be sufficient. For that reason the simulations in Section 4.3 were dealt through a steady-state flow analysis.

For the competition, as referred in Section 2.2.3, cars reach a maximum of around 120 km/h that is close to 0.1 Mach, well below the labeled value of 0.3 Mach, from which air is considered to be compressible.

From this, it is possible to avoid using the energy conservation equation, since there are only two unknowns, (p and \mathbf{V}) for two equations, continuity and momentum, that based on the referred assumptions can be listed simply as

$$\nabla \cdot \mathbf{V} = 0 \text{ and} \quad (3.9)$$

$$\nabla \cdot (\rho \mathbf{V}) \mathbf{V} = -\nabla p + \mathbf{F}_{Viscous} \quad (3.10)$$

or, in integral form,

$$\iiint_v \nabla \cdot (\rho \mathbf{V}) dv = 0 \text{ and} \quad (3.11)$$

$$\iiint_v \nabla \cdot (\rho \mathbf{V} \cdot \mathbf{V}) dv = - \iiint_v \nabla p dv + \mathbf{F}_{Viscous} \quad (3.12)$$

Equations (3.11) and (3.12) are, respectively, the continuity and momentum equations used in all subsequent chapters in this thesis.

There is one more possible simplification of the governing equations, where the effects of viscosity are negligible (inviscid flow), which would result in the Euler equations. These type of simplifications are not appropriate to the problem at hand, since the viscous forces play an important role and are not dominated by inertial forces. Although, for example for a high speed projectile, this type of simplifications can be made with the purpose of lowering the complexity of the problem for the first iterations.

3.2 Finite Volume Method

Numerical simulation software packages use a defined volume of interest and split it into small control volumes ν , thus creating a superficial or volume mesh. Finite volume method (FVM), like the finite element method (FEM), is suitable for irregular and complex geometries.

FVM has an advantage over FEM for fluid simulations, as it is based on the integral form, in contrast to the differential form used in FEM, which is based on PDEs. This results in more accurate and stable methods, especially when solving models who suffer from high gradient state variables (i.e. large derivatives) that can occur in flow recirculation. The integral form conservation laws applied to each individual finite volume, to form enough algebraic equations so that the conservation equations can be solved while iteratively computing the dependent variables.[15, 16]

ANSYS Fluent 19, the CFD program used in Chapter 4, is a Green-Gauss Finite Volume Method with a Cell-Centered formulation. This means, that ANSYS Fluent uses an algebraic form of the integral conservation equations, Equations (3.11) and (3.12), applied to each small control volume (CV) as well as the solution domain as a whole. "If we sum equations for all CVs, we obtain the global conservation equation, since the surface integrals over inner CV faces cancel out. Thus, global conservation is built into the method" [13].

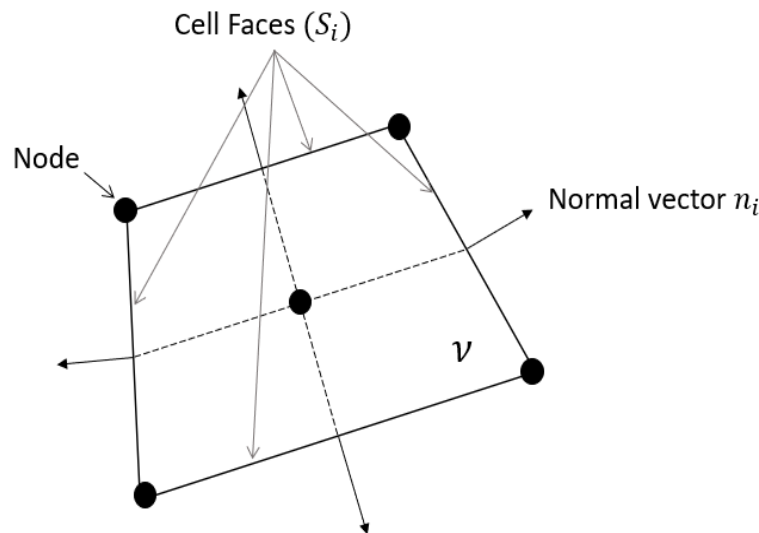


Figure 3.2: Typical polygonal 2D cell.

In Figure 3.2 it can be seen a typical cell/ control volume which will be taken as an example for the sake of better reasoning. Taking its notations for the deduction of the mentioned algebraic variation and applying the Green-Gauss method to both Equations (3.11) and (3.12) it is possible to obtain the following equations

$$\sum_i \oint_{S_i} \rho V \cdot \mathbf{n}_i dS = 0 \text{ and} \quad (3.13)$$

$$\sum_i \oint_{S_i} \rho V \cdot V \cdot \mathbf{n}_i dS = -\nabla \bar{p} \cdot \nu + \mu \sum_i \oint_{S_i} \nabla V \cdot \mathbf{n}_i, \quad (3.14)$$

for $\mu \nabla \cdot \mathbf{V} = \mathbf{F}_{Viscous}$.

where μ is the dynamic viscosity, \mathbf{n}_i is the surface S_i unitary outward normal vector and ν the cell volume.

From this, it is possible to obtain the approximated algebraic expressions, from which instead of calculating the field variables in all the points of the domain the integral is approximated in terms of one or more locations of the cell faces. As referred above, ANSYS Fluent uses the cell centered value which itself is an approximation of the mean value over the surface. Since the values of the field variables are not available in the cell center, this is obtained through interpolation of the control volume corner (nodes) values and the usage of shape functions.

3.3 Computing Forces

Aerodynamic forces play an important role in the simulation world, being used both as a model performance measurement and as a convergence checking of the simulation as it will be possible to confirm in Section 4.4.2.

ANSYS Fluent is able to calculate the total force component of a specified surface vector on a wall zone, through the sum of the dot product of the pressure and viscous forces on each face with the specified force vector.[17] The terms in this summation represent the pressure and viscous force components in the direction of vector \vec{a} :

$$F_a = \vec{a} \cdot \vec{F}_p + \vec{a} \cdot \vec{F}_v \quad (3.15)$$

where

$$\begin{aligned} \vec{a} &= \text{specified surface vector} \\ \vec{F}_p &= \text{pressure force vector} \\ \vec{F}_v &= \text{viscous force vector.} \end{aligned}$$

The total force component will be computed for each of the selected wall zones and consequently for each cell within. To reduce round-off errors a reference pressure is used to normalize the cell pressure, for example

$$\vec{F}_p = \sum_{i=1}^n (p - p_{ref}) A \hat{n} \quad (3.16)$$

for the net pressure vector it can be computed through Equation (3.16) where n is the number of faces, A is the area of the face and \hat{n} is the face unit normal.

3.4 Boundary layer

The boundary layer is an important part of the flow around an object, since the frictional force between the flow and the object will retard their relative motion, the object surface is exposed to a shear stress (τ), and on the other hand, as an opposite reaction, the flow will decrease its local velocity. The boundary layer plays an important role in airfoil theory, being the main cause of aerodynamic forces, Figure 3.3.

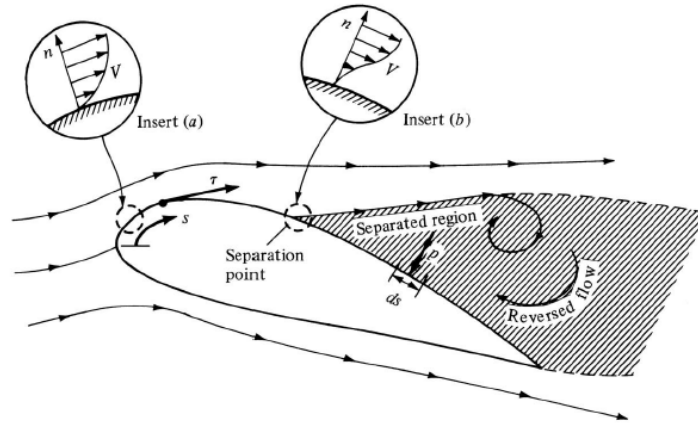


Figure 3.3: Boundary layer around an airfoil [12].

At near wall regions, the fluid tends to work in a different way from the rest of the fluid domain, that is due to viscosity. This results in a high velocity gradient in the vicinity of the contact zone, since, on the wall, the relative velocity between the fluid and the wall will be equal to zero (no-slip condition).

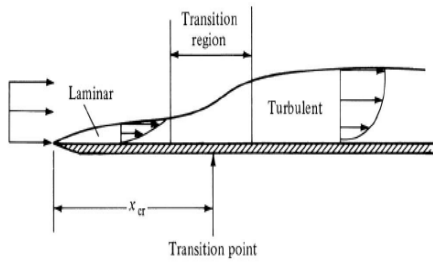


Figure 3.4: Boundary layer regions[12].

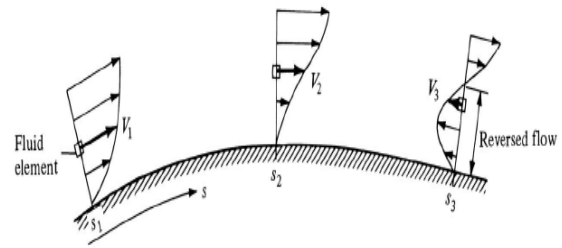


Figure 3.5: Velocity profile for a reversed flow [12].

The boundary layer can be divided into three different components, as represented in Figure 3.4, the laminar region, the turbulent region and between them, as the name says, the transition region.

All these regions exhibit different characteristics, the way to distinguish them being the Reynolds number, the relation between inertial and viscous forces. A critical Reynolds number, Re_{cr} , indicates the position x_{cr} where the laminar to turbulent flow transition may occur.

One of the main differences between the turbulent and the laminar regions is the velocity profile. "Because of the agitated motion in a turbulent flow, the higher-energy fluid elements from the outer regions of the flow are pumped close to the surface. Hence, the average flow velocity near a solid surface is larger for a turbulent flow in comparison with laminar flow." [12], which can be written as

$$\left[\left(\frac{\partial V}{\partial n} \right)_{n=0} \right]_{Turbulent} > \left[\left(\frac{\partial V}{\partial n} \right)_{n=0} \right]_{Laminar} \quad (3.17)$$

where n is the coordinate normal to the surface. Due to the differences on the velocity profile, both types of flow are beneficial in distinct types of applications. Turbulent flow can be used to lower the profile drag, the sum of pressure and skin friction drag, in blunt bodies since the main source of drag comes from the pressure difference and for a turbulent flow the energy of the fluid elements close to the surface is larger and because of that it doesn't separate from the surface as readily as a laminar flow. However for a more slender body a laminar boundary layer would be more beneficial since the main source of Drag would come from the friction component.

Another phenomenon present in boundary layers is the reversed flow illustrated at station S_3 in Figure 3.5. "If the fluid element is focused and followed as it moves downstream. The motion of the element is already retarded by the effect of friction; in addition, it must work its way along the flow against an increasing pressure, which tends to further reduce its velocity. Consequently, at station 2 along the surface, its velocity V_2 is less than V_1 . As the fluid element continues to move downstream, it may completely "run out of steam," come to a stop, and then, under the action of the adverse pressure gradient, actually reverse its direction and start moving back upstream." [12] This type of phenomenon usually occurs when the body surface has steep angles or high cambers like the one illustrated in Figure 3.5.

Turbulent boundary layer analysis

Taking a closer look into the normal development of the velocity profile in a wall-bounded flow, three distinct regions within the boundary layer can be listed, Figure 3.6. Where through a logarithmic representation of the dimensionless variables, y^+ and U^+ it is possible to obtain a general profile of the turbulent boundary layer, valid for a different range of bodies and flows. The dimensionless variable y^+ , which is the dimensionless normal distance from the surface, and U^+ , which is the dimensionless velocity, can be defined by Equations (3.18) and (3.19), respectively,

$$y^+ = \frac{y u_\tau}{\nu} \quad (3.18)$$

$$U^+ = \frac{U}{u_\tau} \quad (3.19)$$

where u_τ is a reference velocity based on the wall shear stress, defined as $\sqrt{\tau_{wall}/\rho}$, and ν is the fluid kinematic viscosity.

"Very close to the wall, viscous damping reduces the tangential velocity fluctuations, while kinematic blocking reduces the normal fluctuations. Toward the outer part of the

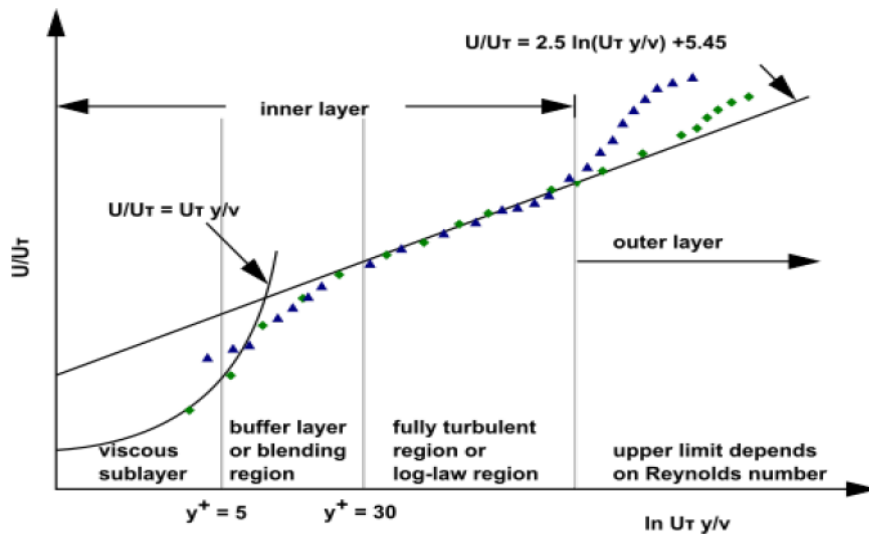


Figure 3.6: Boundary layer subdivisions [17].

near-wall region, however, the turbulence is rapidly augmented by the production of turbulence kinetic energy due to the large gradients in mean velocity.” [17].

The innermost layer is called the viscous sublayer, $y^+ < 5$, where the flow is almost laminar and viscous effects play a dominant role in momentum and heat or mass transfer. The log-law region or fully turbulent region, $y^+ > 30$, is the outer portion of the inner layer, in which turbulent shear stress plays a major role since it is close enough from the wall surface for inertial forces to be neglected, yet distant enough for the viscous forces to be negligible, while the in between region of the viscous sublayer and fully turbulent layer is called buffer layer, where both molecular viscosity and turbulence effects are equally important. Finally, the outer layer keeps a similar behaviour to the one found in the fully turbulent region until it reaches the free flow air velocity, and its upper limit will be defined by the Reynolds number.

3.5 Turbulence models

In order to simulate the flow’s turbulence processes, a Reynolds averaging method is applied to the instantaneous Navier-Stokes, Equations (3.9) and (3.10).

The Reynold Averaging Navier-Stokes (RANS) can then be obtained through the division of the air velocity into two components,

$$u_i = \bar{u}_i + u'_i \quad (3.20)$$

where \bar{u}_i and u'_i are the mean and fluctuating velocity components ($i = 1, 2, 3$), for a 3D evaluation. The RANS equations have the same general form as the instantaneous Navier-Stokes equations, with the velocities and other solution variables now representing ensemble-averaged (or time-averaged, non-fluctuating) values. An additional term appears from the convective terms, called Reynolds stresses, $-\rho \overline{u'_i u'_j}$.

In order to model the Reynolds stresses correctly, the Boussinesq hypothesis [18] is used to relate the flow with the mean velocity gradients, as

$$-\rho \overline{u'_i u'_j} = \mu_t \left(\frac{\partial \overline{u}_i}{\partial x_j} + \frac{\partial \overline{u}_j}{\partial x_i} \right) - \frac{2}{3} \left(\rho k + \mu_t \frac{\partial \overline{u}_k}{\partial x_k} \right) \delta_{ij} \quad (3.21)$$

in which a new unknown appears, the turbulent viscosity, μ_t . The turbulent models have the responsibility of proposing and solving additional transport equations for additional variables, from which is obtained the turbulent viscosity. Depending on the turbulence model, one or two transport equations are used for that purpose. For example in the case of the Spalart-Allmaras model, only one additional transport equation is solved. While in the case of the $k - \epsilon$ and $k - \omega$ models, two additional transport equations (for the turbulent kinetic energy, k , and either the turbulent kinetic energy dissipation rate, ϵ , or the specific dissipation rate, ω) are solved.

From what was possible to observe from the literature [17, 4, 19, 20] and some initial experimenting with the turbulence models, for the type simulation on hands, where a high pressure gradient is expected, two turbulence models were usually taken as the best approaches, the Spalart-Allmaras model and the SST variation of the $k - \omega$ model.

"The Spalart-Allmaras model was designed specifically for aerospace applications involving wall-bounded flows and has been shown to give good results for boundary layers subjected to adverse pressure gradients. It is also gaining popularity in turbo-machinery applications." [17]

"The SST $k - \omega$ model includes all the refinements of the BSL $k - \omega$ model, and in addition accounts for the transport of the turbulence shear stress in the definition of the turbulent viscosity. These features make the SST $k - \omega$ model more accurate and reliable for a wider class of flows (for example, adverse pressure gradient flows, airfoils, transonic shock waves) than the standard and the BSL $k - \omega$ models." [17]

Chapter 4

Car CFD simulation process

To accomplish the needed results for the rear wing optimization a simulation of the car forward part is essential. For that ANSYS Fluent 2019 software was chosen. In addition to that, the computer-aided design (CAD) software SOLIDWORKS was also used to replicate the car geometry.

In this chapter, it is possible to find a description of the car model simulation process, working as starting point for the rear wing optimization. The choices and simplifications made in this chapter were supported by the theoretical issues addressed in Chapter 7.

4.1 Model preparation

The first challenge encountered during the pre-processing was to create a simplified, solid bodied model in which the unnecessary details would be removed without compromising the CFD results. The car CFD model was made with the CAD software SOLIDWORKS, respecting the overall geometry and measurements of the real car, Figure 4.1.

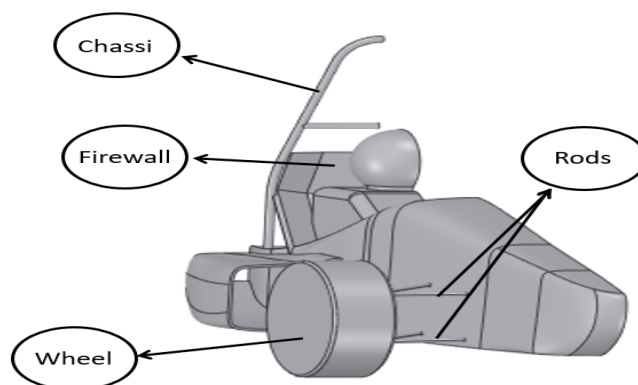


Figure 4.1: Car CAD model.

For this model all the parts from the powertrain were not considered, the A-arms, suspension and tyres were critically simplified and only half of the car was modeled due

to its symmetry relative to the middle plane longitudinal axis. This model adaptation resulted in a relevant decrease of the analysis complexity level, and consequently a decrease on computational time while keeping the essential for the analysis intended in this work.

The CAD model was saved in a IGS type file and imported into ANSYS Space Claim, where small surface corrections were made to the model in order to avoid gaps, extra edges or missing faces for the creation of the enclosure represented in Figure 4.2. The enclosure dimensions suffered changes during the process, increasing its size gradually up to a final size of 22,2x3,7x4,5m (*Length x Height x Width*), (in Figure 4.2 L is the length of the car model). A refined BOI (Body Of Influence) was created to better solve the flow characteristics around the car model reaching a total size of 10.2x2.9x2,7m (*Length x Height x Width*), and represented in darker grey in Figure 4.2.

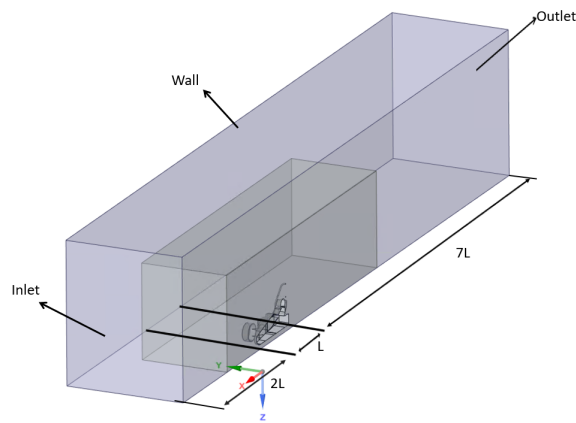


Figure 4.2: Enclosure and body of influence.

Another adaptation made, now to the model enclosure, was the creation of rounded edge between the ground and tyre with the purpose of ensuring contact between both so that air flow wouldn't go under the tyre, Figure 4.3.

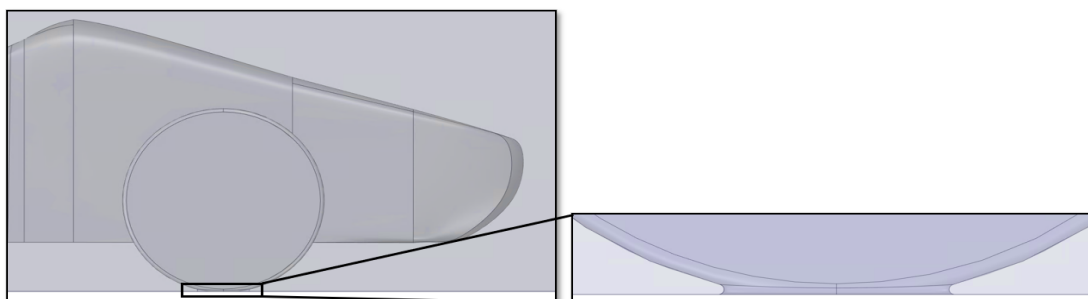


Figure 4.3: Wheel/ground interaction.

4.2 Meshing

4.2.1 Surface mesh

As mentioned in Section 3.2, ANSYS Fluent is a software based on the Finite Volume Method which uses an unstructured mesh algorithm to define the small control volumes. The meshing process can be initiated through the definition of a generic cell size range, controlling only the minimum and maximum size values and the cells growth rate. This first mesh iteration is represented in Figure 4.4.

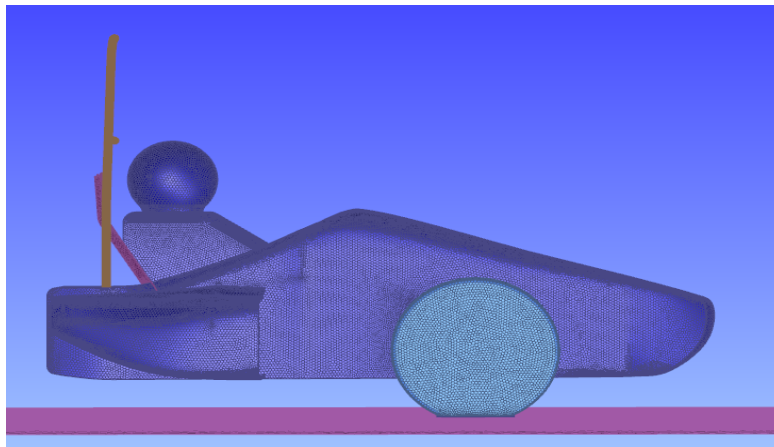


Figure 4.4: First iteration of the Car surface mesh (lateral view).

Size functions or scoped sizing controls

Since the generic surface mesh revealed to be insufficient for some car surfaces, a more refined surface mesh was needed in specific locations. For that, ANSYS Fluent uses size functions that enable a specific type of surface mesh in a chosen selection. In this particular case this functionality was used to refine the mesh applied to the rods, firewall, wheel, chassi and remaining car model.

Three types of size functions were used to bypass the problems raised by the generic mesh:

- Body of influence (BOI)
- Curvature
- Proximity

Body of influence

The body of influence size function enables the specification of a mesh refinement for a closed region where it is possible to define a maximum cell size and the minimum cell size will be determined based on the influence of other size functions [21]. In Figure 4.5 the body of influence refinement can be seen in both symmetry and ground surfaces.

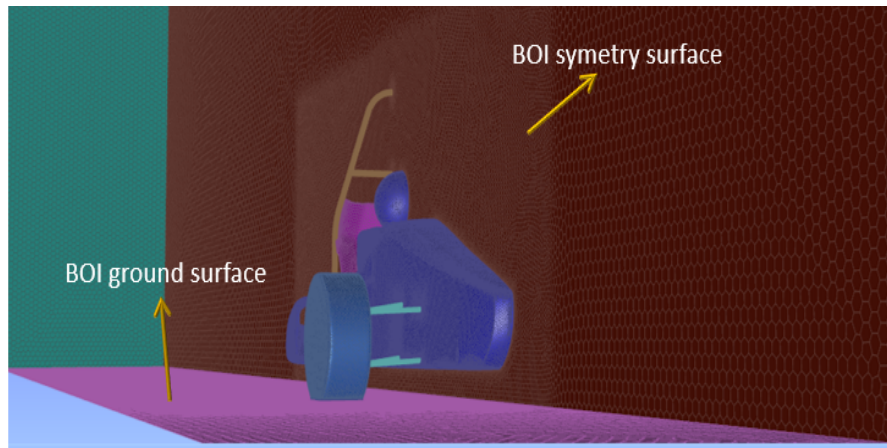


Figure 4.5: BOI consideration in the car and enclosure surface mesh.

Curvature

"The curvature size function/scoped control computes edge and face sizes using their size and normal angle parameters, which are either automatically computed or defined." [21]. This size function type revealed to be useful in almost all regions of the model, since it allowed to control the level of mesh refinement in high angled curves. For example, for a normal angle value of 5° , within the curvature size function, the cell division was made when the angle change along the curve is 5° , meaning that a 80° arc will be divided into approximately 16 segments.

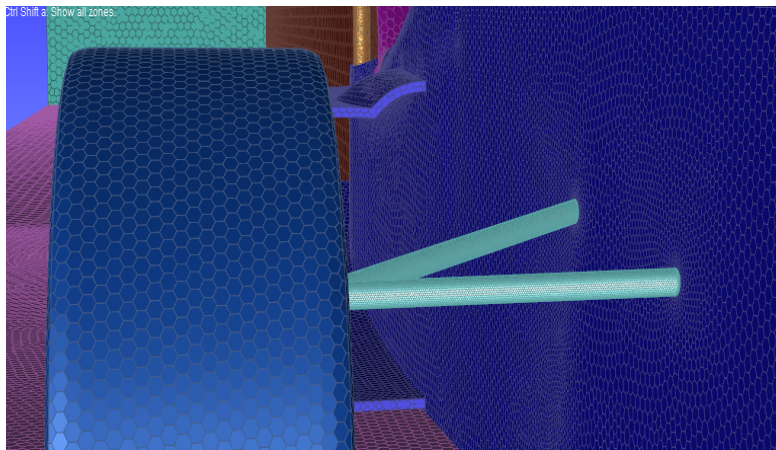


Figure 4.6: Wheel and suspension rods surface mesh refinement.

Proximity

"The proximity size function/scoped control computes edge and face sizes in 'gaps' using the specified minimum number of element layers. For the purposes of specifying proximity sizing, a 'gap' is defined in one of two ways:

- The area between two opposing boundary edges of a face
- The internal volumetric region between two faces"[21].

The proximity size function was used on the firewall specially because of the face boundary option, which computes the edge-edge proximity within each face, being particularly useful for thin plates like the firewall where initially other size functions weren't able to successfully replicate its corners.

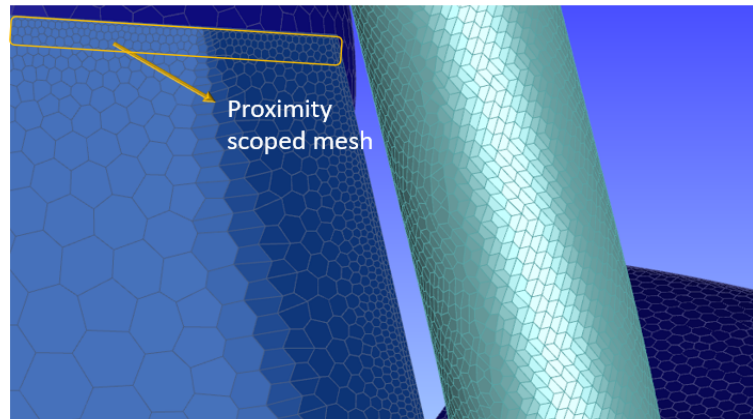


Figure 4.7: Firewall and chassis surface mesh refinement.

After application of the referred refinements, the next step went through a confirmation of the surface mesh quality and face connectivity, which can be evaluated by the following parameters:

- Free-faces
- Multi-faces
- Duplicate-faces
- Skewed-faces
- Aspect ratio

The evaluation of the free-, multi-, and duplicate faces is used as way of checking if the surface mesh has no leakage or critical malfunction which wouldn't allow the creation of fluid volumetric regions. For the measurement of mesh quality both skewed-faces and aspect-ratio can be used, where usually high values of skewness and aspect ratio lead to worst results. The aspect ratio can be simply described as the ratio between the longest edge length to the shortest edge length, while the cell skewness can be measured by

$$Skewness = \frac{\text{Optimal cell size} - \text{cell size}}{\text{Optimal cell size}} \quad (4.1)$$

where the optimal cell size is the size of an equilateral cell with the same circumradius. The value used as a limit of skewness quality was 0.9. This value was taken from [21], as for higher values the quality of the cell is considered bad.

After the process described in this chapter the model was ready to be submitted for a volume mesh. It is important to highlight that this process was repeated for each mesh iteration made for this simulation.

4.2.2 Volume mesh

"Computational Fluid Dynamics (CFD) solvers are more efficient with a highly orthogonal mesh, yet geometries are steadily increasing in complexity and it can be difficult to achieve or thogonality on irregular geometries. Each element type has its pluses and minuses, so CFD meshing technology has evolved over the past four decades to use different types of elements that are best suited for specific application spaces. Engineers want to match the optimal mesh elements for each area of the geometry and volume, but building the transition between these areas can be a difficult challenge. As a result, they may use fewer element types than optimal in order to reduce time and effort to acceptable limits".[22]

For the creation of the volume meshes, four different types of cell geometries were available as a possibility:

- Tethahedral
- Hexcore
- Polyhedral
- Poly-hexcore

The cells geometries that revealed to be more accurate to replicate the model were the polyhedral and hexcore cells that can be stitched into the same mesh through the Ansys Fluent mosaic technology (Poly-hexcore), which automatically connects different types of meshes with polyhedral elements.

"Poly-Hexcore, the first application of Mosaic technology, fills the bulk region with octree hexes, keeps a high-quality layered poly-prism mesh in the boundary layer and conformally connects these two meshes with general polyhedral elements."[22]

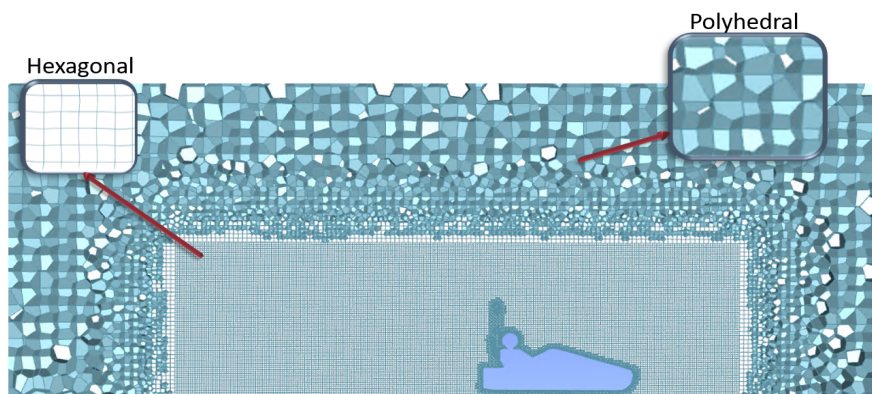


Figure 4.8: Volume mesh section view.

Polyhedral cells appear to have a specially good performance when handling high gradient fluid flows because of their extensive neighbors, usually around 10. Meaning

that even while using linear shape functions and a small number of cells it is possible to obtain good results. For this reason, in a poly-hexcore mesh the polyhedral type cells can be found near the car surfaces and can also work as a connection between the boundary layer prism type and the hexcore cells. The hexahedral elements are not well suited for complex geometries but demand smaller meshing computational power, due to their simpler geometry when compared with polyhedral cells. For that reason most of the refined fluid domain present in the BOI was filled with a hexagonal cells, as can be observed in Figure 4.8, while the non refined part of the domain was filled with polyhedral cells.

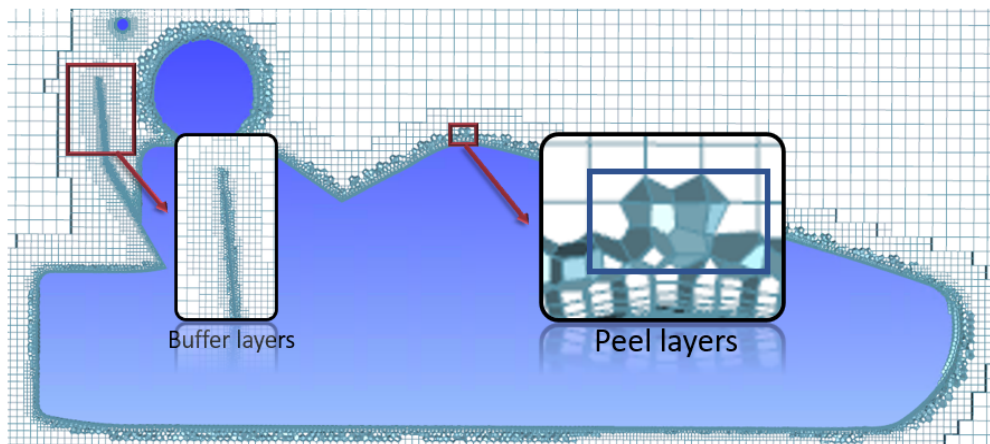


Figure 4.9: Volume mesh transition layers.

The buffer layers have the purpose of alleviating rapid transitions from finer to coarser cells and can achieve that with additional layers of cells between the cells with a disparity in size. Peel layers are additional layers that are able to control the gap between the hexahedral core and the geometry; in this case, polyhedral cells are used to fill the additional layers between the prisms chosen for the boundary layer and the hexahedral core.

The number of both buffer and peel layers were the two parameters used to control the amount of additional layer, which are hold responsible for the transitions between diverse types of cells. The values chosen were 3 buffer layers and 1 peel layer, and were used for all the mesh iterations approached on this thesis.

A boundary layer mesh option was added in order to complement the poly-hexcore mesh where, through poly-prism layer growth layer and a near wall model approach, it was possible to facilitate the replication of the boundary layer phenomena described in Section 3.4.

The size of the first prism cell on the boundary layer was obtained by an iterative process using the y^+ value, estimated from the preliminary post-processing of the simulation, as described in Section 4.4.1.

Finally, a similar approach to the one used for the surface mesh, each iteration of the volume mesh went through a quality assessment, where graphics like the one exposed in Figure 4.11 were plotted to make decisions. The number of cells is represented through a logarithmic scale on the y-axis and the skewness value on the x-axis. For all the volume meshes approached on this thesis, the skewness values were always smaller

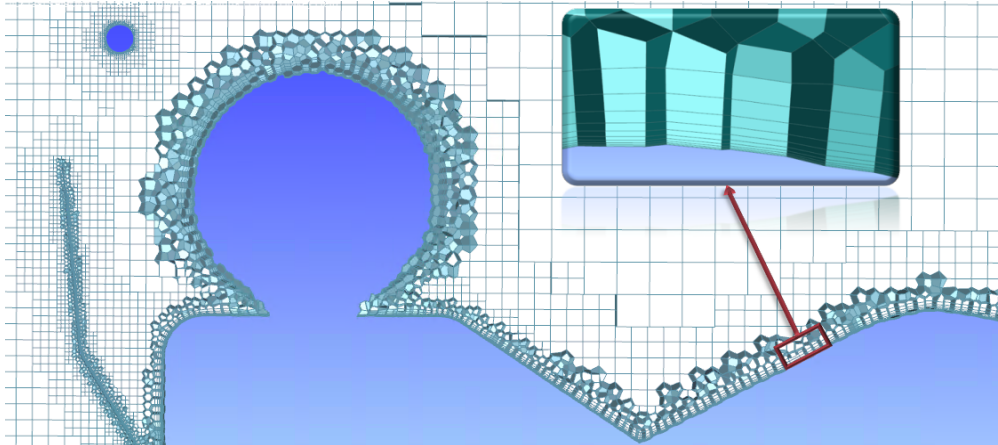


Figure 4.10: Volume mesh section view boundary layer poly-prims.

then 0.9, the highest admittable value of this procedure even so, most of the cells had a skewness value close to 0.1.

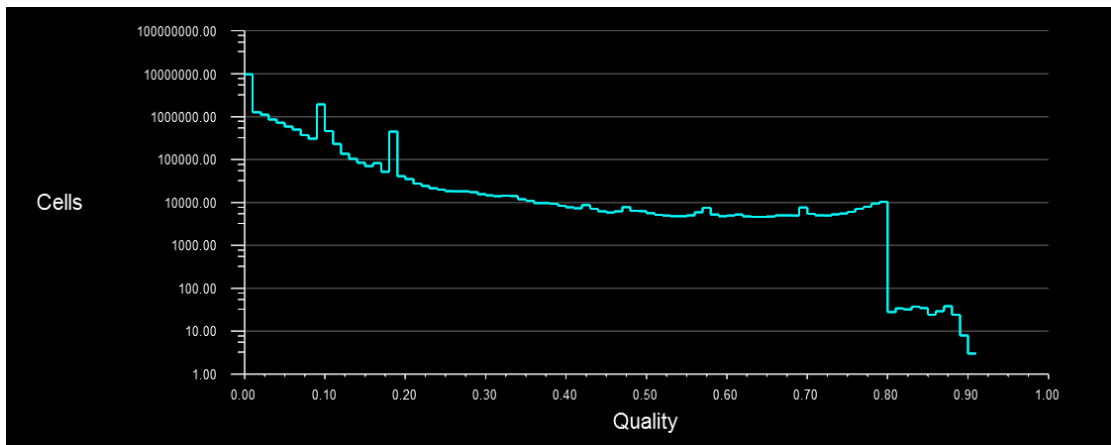


Figure 4.11: Number of cells vs skewness.

4.3 Setup and boundaries

After the final assessment of the volume mesh quality, the model was prepared for the last step of the pre-processing. The setup is the section in which is possible to choose and apply the best fitting strategy and equations for the problem at hand, while controlling both solution methods and iterative coefficients affecting the convergence and the strategy used to calculate the dependent variables. It is also possible to define the boundary conditions and reference values that enable the calculation of the aerodynamic forces, Lift (L) and Drag (D), and consequently their associated non-dimensional coefficients, C_l , C_d , and even the Reynolds number (Re).

4.3.1 Turbulence model

Although both models led to similar results, the Spalart-Allmaras model showed lower levels of residuals and a better convergence for the non-dimensional coefficients, and for that reason the Spalart-Allmaras turbulence model was initially selected. Therefore, the mesh independence studies carried out in Section 4.4.2 were done while using the Spalart-Allmaras model. However, since the SST $k - \omega$ model was considered the most well established of the two methods for open wheel car configurations [17, 4, 19, 20], in order to better verify the results obtained through the Spalart-Allmaras turbulence model a simulation with the SST $k - \omega$ turbulence model as the viscous model was carried out while using the converged mesh originated from the mesh convergence study.

4.3.2 Boundary conditions and reference values

There are points of the enclosure under analysis for which is possible to premeditatedly attribute velocity or pressure values. These values were assigned to its corresponding selections based on the theoretical expectations of the model and observation of similar simulations. For example, in the boundary conditions used for this simulation, which can be found in Table 4.1, it is possible to assign a null velocity to the car faces (no slip-wall condition, based on the theoretical background stated in Section 3.4).

Table 4.1: Boundary Conditions.

Named Selection	Boundary Condition
All Car Faces	No-Slip Wall
Ground and Enclosure walls	Moving Wall at V_{in} (m/s)
Inlet	V_{in} (m/s)
Outlet	0 Gauge Pressure Average Pressure
Symmetry	Symmetry Condition
Wheel	Rotating Wall Speed= V_{in}/r (rad) Axis Origin Rotating Axis -+

It is possible to control the reference values that are used in the computation of derived physical quantities and non-dimensional coefficients. These reference values (Table 4.2) are used for the solution component of the simulation, and in this thesis will be used to calculate the non-dimensional coefficients C_l , C_d , and even the Reynolds number (Re).

The density and viscosity values correspond to the air characteristics at 15 °C and 1 atm, and were left as default and the flow velocity was considered approximately equal to V_{in} . The frontal area was calculated with the the help of SOLIDWORKS, following the same approach as in Hucho (1993) [23], and can be found represented in blue in Figure 4.12.

Table 4.2: Fluid flow reference values.

Reference Values for ANSYS Fluent					
<i>Frontal Area</i> (m ²)	ρ (kg m ⁻³)	μ (kg (m·s) ⁻¹)	U (m·s ⁻¹)	V_{in}	<i>Length</i> (m)
0.467	1.225	$1.7894 \cdot 10^{-5}$			2.2

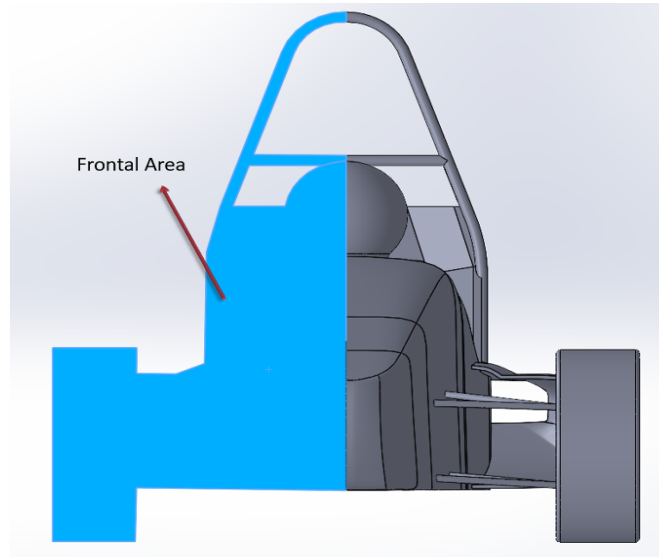


Figure 4.12: Frontal area of half of the car.

4.3.3 Solution methods and controls

Regarding the Fluent solver, three-dimensional and steady-state conditions were defined for the CFD simulations. Transient conditions could have been used and investigated, since it would have been in the field of interest of this thesis, although it would imply a considerable increase in computational time.

The chosen method to solve the continuity and momentum governing equations was the pressure-based solver, that allows the user to solve its CFD problem in either a segregated or coupled manner. For this simulation, a coupled approach was taken as reference due to what was found in the Ansys Fluent Theory Manual [17]: "The coupled scheme obtains a robust and efficient single phase implementation for steady-state flows, with superior performance compared to the segregated solution schemes".

Solver settings and solutions methods described above were applied in all CFD simulations performed for this thesis.

Table 4.3: Spatial discretization schemes selected for the numerical analyses in ANSYS Fluent while using the Spalart-Allmaras turbulence model.

Gradient	Least Squares Cells Based
Pressure	Second Order
Momentum	Second Order Upwind
Modified turbulent viscosity	Second Order Upwind

Table 4.4: Spatial discretization schemes selected for the numerical analyses in ANSYS Fluent while using the SST $k - \omega$ turbulence model.

Gradient	Least Squares Cells Based
Pressure	Second Order
Momentum	Second Order Upwind
Turbulent Kinetic Energy	Second Order Upwind
Turbulent Dissipation Rate	Second Order Upwind

As referenced in Section 3.2, ANSYS Fluent uses a co-located scheme, whereby pressure and velocity are both stored at cell centers instead of at all the nodes, which means that for an evaluation of the field variables at the full face a reconstruction needs to be made.[17]

For the interpolation of the values on the mesh faces, a second order scheme was chosen. This type of scheme uses a central differencing technique, which can be found in detail on Ansys Theory Manual [17], and revealed to have an improved accuracy when compared to the linear and standard schemes, specially in zones with high gradients of the field variables (Tables 4.3 and 4.4).

As referenced before, the solver goes through an iterative process to achieve the desired results. In Ansys Fluent it is possible to control some of the variables in order to obtain better results. Solver settings and solution controls were left as default in all CFD simulations performed, with exception of the Flow Courant number that suffered some adjustments for each specific simulation.

The Courant number (C) or CFL can be defined as the number of cells that the flow "moves" in a certain artificial time step (Δt), Equation 4.2. Even though the simulation operates in a steady state regime and the pressure-based solver works with an implicit method, there will be some regions in which the field variables' values will fluctuate with time, due to turbulence. Therefore, in order to capture the small perturbations caused by turbulence, the Courant number can be used to manipulate the amount of times the solver checks the field variables.

$$C = \frac{\text{Fluid distance}}{\text{Cell distance}} = \frac{U\Delta t}{\Delta x} \quad (4.2)$$

4.4 Results and post-processing

4.4.1 y^+ value and boundary layer definition

As referred at the end of Section 4.2.2, in order to achieve a viable first cell height of the boundary layer prism cells an iterative method based on the y^+ was embraced. The initial guess for the y_p value, which is the distance from the cell centroid to the wall surface, was calculated for a simplified flow over a flat plate which Reynolds number can be estimated by,

$$Re = \frac{\rho UL}{\mu} \quad (4.3)$$

where L is the car length and U the inlet velocity. With the knowledge of the Reynolds number, the fully turbulent skin friction formula was used (Eq. 4.4), to obtain the wall

shear stress (Eq. 4.5), and consequently the friction velocity (Eq. 4.6)

$$C_f = [2 \log_{10}(Re) - 6.5]^{-2.3} \quad (4.4)$$

$$\tau_w = \left(\frac{1}{2} \rho U^2\right) C_f \quad (4.5)$$

$$u_\tau = \sqrt{\frac{\tau_w}{\rho}} \quad (4.6)$$

from which the value of y_p can be computed through the following equation,

$$y_p = \frac{y^+ \mu}{\rho u_\tau} \quad (4.7)$$

for which y^+ was attributed the value of $y^+ = 1$, since ideally that would be the overall value of the boundary layer. As in ANSYS the value needed for meshing the boundary layer zone is the first cell height, y_H , and not the centroid height, the conversion was made by $y_H = 2 \cdot y_p$.

After the initial value of y_H was assured, the following iterative process represented in Figure 4.14 was followed.

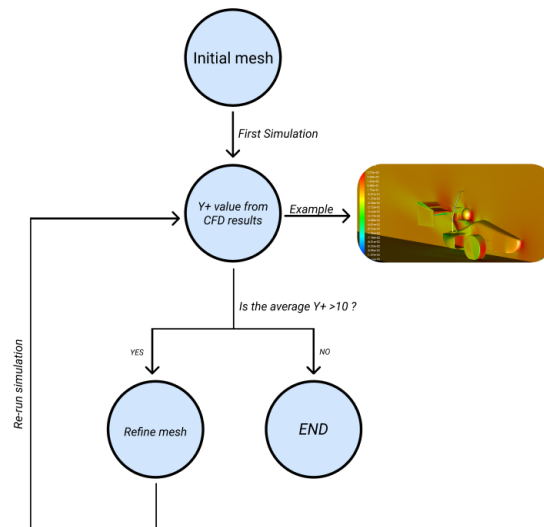


Figure 4.13: Scheme of the y^+ iterative process.

Following this process it was possible to obtain an average value of 2.3 for y^+ around the car main body surface, with a value of 1.25×10^{-5} m for y_p and 20 layers of prisms on the boundary layer zone.

However, even more important than achieving certain y^+ values, is to ensure that the prismatic layers enfold the car boundary layer in its total height, and test simulations were executed to define a suitable growth rate and number of prismatic layers. At the end of each test simulation the turbulence viscosity ratio was checked in the symmetry plane, in which near the car surface the turbulence viscosity ratio is expected to be

low and increase gradually until the end of the boundary layer where a steep decrease should occur, from what was described in the normal development of a boundary layer in Section 3.4. Additionally, according to ANSYS Fluent theory guide (2021)[17] the maximum turbulent viscosity occurs in the middle of the boundary layer, implying that twice the location of the maximum turbulent viscosity gives the boundary layer edge.

Both assumptions were taken into account during the test simulations arriving to a final prism layer similar to the one represented in Figure 4.14.

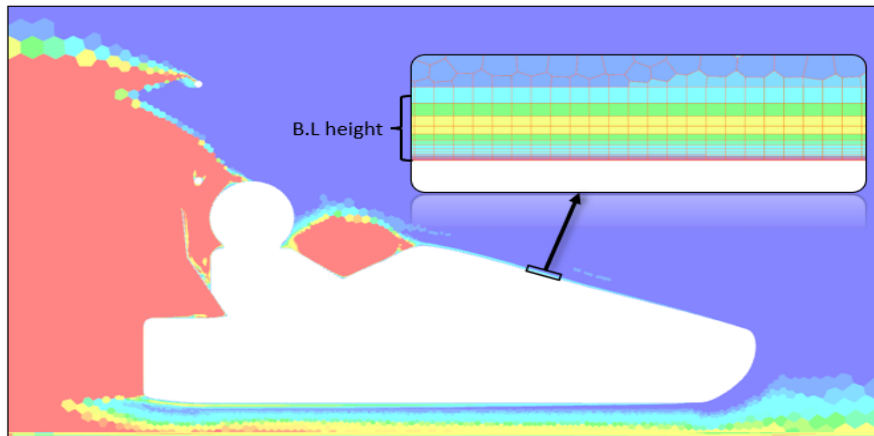


Figure 4.14: Symmetry plane contour of the turbulence viscosity ratio.

4.4.2 Mesh independence studies

The level of accuracy for a simulation can be determined from the relative gradients of mass, velocity or pressure on the domain, and by the convergence of monitored forces as the lift and drag coefficients.

In order to evaluate the quality of the model and to confirm that the simulation is fully converged and does not depend significantly on mesh resolution, mesh independence studies were conducted. The study was done by holding the mesh used in the first simulation, that showed trustworthy results, as a central point and testing both more refined and coarser meshes, while keeping the calculated C_l and C_d under observation. A simulation, under this thesis, was considered trustworthy when all the relative residuals revealed to be under the 10^{-3} margin and the non-dimensional lift and drag coefficients showed a variation within the 1% margin for at least 100 iterations on both C_l and C_d .

Due to the high computational effort and time cost of running a full simulation of this model only 3 more meshes were tested for the same setup with the Spalart-Allmaras turbulence model, Figure 4.15.

This procedure has the purpose of achieving results that are accurate enough while keeping the computation times to a minimum, and from Figure 4.15 where the C_l values are represented in red and the C_d values in blue the mesh with 20 million cells was chosen as the optimal mesh. The chosen mesh was then used with the SST $k - \omega$ turbulence model resulting in $C_l = -0.23$ and $C_d = 0.77$, which corresponds to a 2% deviation in both variables when comparing to the Spalart-Allmaras results.

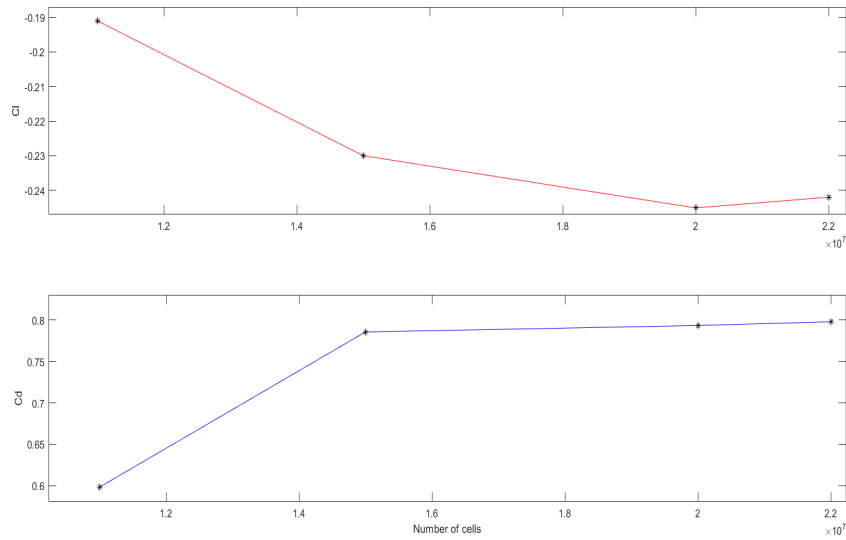


Figure 4.15: C_l and C_d values for tested meshes.

4.4.3 CFD results

Through a close observation of the pathlines along the car geometry, represented in Figures 4.16 and 4.18, and the velocity contours represented in Figure 4.17, it is possible to conclude that in the mounting zone of the rear wing, defined by the rules, the air flow has a low velocity magnitude and high levels of recirculation due to the low pressure zone created behind the driver and firewall (already expected).

Ideally, the rear wing would be positioned higher enough to avoid this kind of air flow perturbations and be exposed to a high velocity free flow. However, since this isn't possible due to the stipulated competition rules, a formulation of an aerodynamic optimization problem becomes even more interesting and viable because the solutions found by other teams may not be well adapted to this car geometry. So, with the elaboration of an optimization problem, the rear wing can be well adapted to the car and maybe even make use of recirculating air movements to improve its aerodynamic performance.

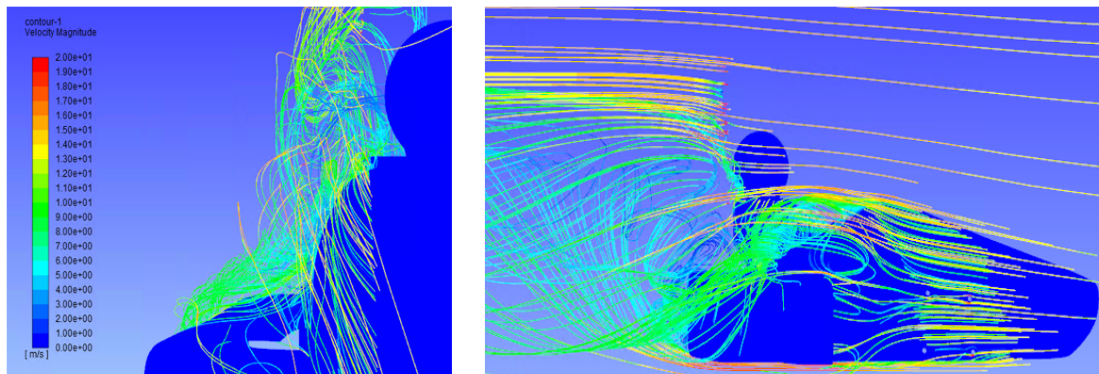


Figure 4.16: Pathlines along the car geometry plane views.

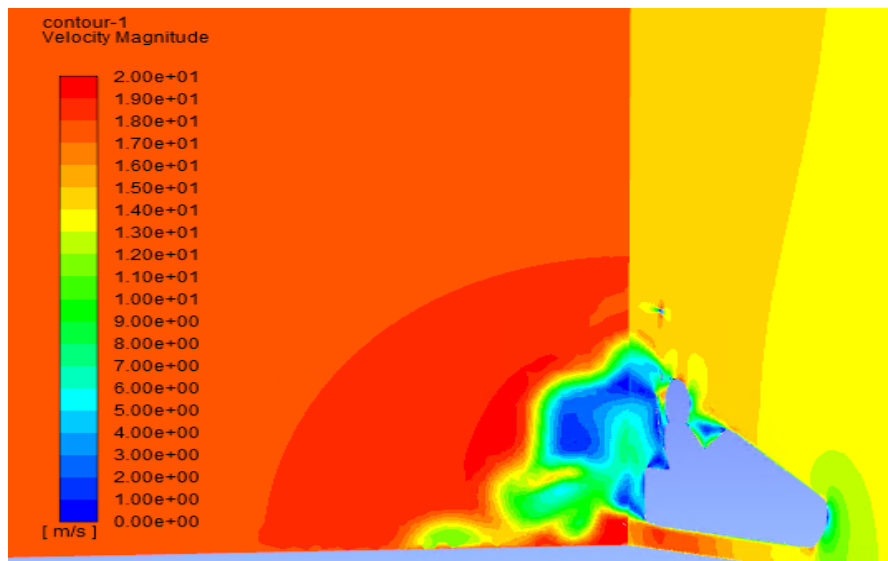


Figure 4.17: Velocity contours on the car symmetry plane and near the rear wing placement region.

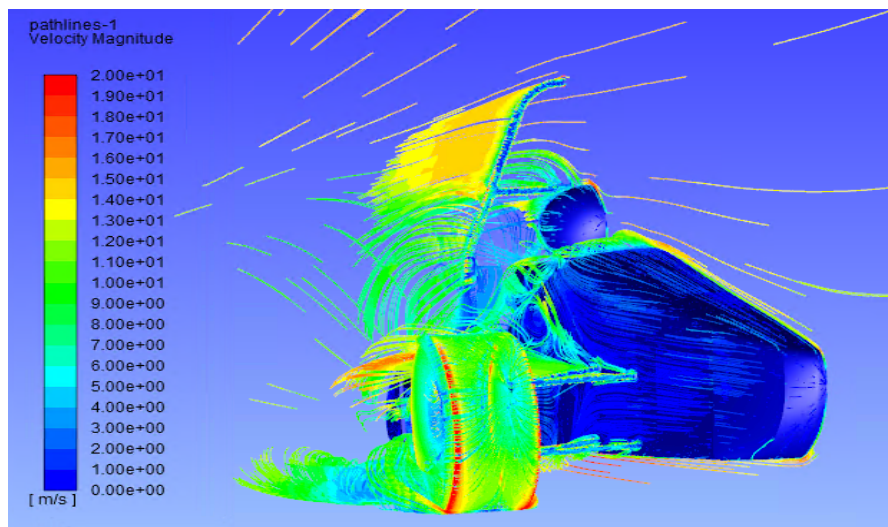


Figure 4.18: Pathlines along the car geometry.

Intentionally blank page.

Chapter 5

Wind tunnel experiments

The wind tunnel experiments, within the scope of this thesis, were performed with the purpose of increasing the validation of the car simulations for lower speeds, by checking the air flow behaviour on a qualitative level.

5.1 Wind tunnel specifications and car model

The wind tunnel experiments were conducted using the facilities of the Atmospheric Aerodynamics Laboratory (AAL) of the Department of Environment and Planning of the University of Aveiro. The wind tunnel is of the open-circuit type with a test section of $6.5m \times 1.5m \times 1.0m$ (with a total length of 12 m), the maximum wind speed in this chamber, with soft and uniform flow, being of 9 m/s (32.4 km/h).



Figure 5.1: Wind tunnel used for the experiments

“The air flow enters the wind tunnel at the intake passing through a flow-straightening section directly to a contraction cone. The honeycomb screen reduces the free stream turbulence level, and the contraction cone increases the airflow velocity towards the test section. Downstream the test section, a coarse-wire mesh and a conical diffuser are linked to the engine constituted by a fan. The diffuser smoothly reduces the air flow velocity without creating turbulence within the test section” [24].

Concluded the analysis of the wind tunnel facility itself, the focus moves to the process of matching the car model installation in the wind tunnel test section to a real world environment, which according to Katz (2006) [25], raises three important issues:

- Simulation of the moving road
- Model size similarity and the blockage it creates
- Mounting of the model and its rotating wheels

Moving roads

The first issue wasn't approached with a solution in this thesis since the wind tunnel didn't possess the necessary equipment to replicate the moving roads.

Model size definition

In order to consider the wind tunnel scale analysis equivalent to the real scale events, both the model and full scale cars must comply with geometric, kinematic and dynamic similarity laws. The geometric similarity was achieved in this experiment since the scaled car model has the same linear scale ratio on all three coordinates of the study area [26]. When it comes to dynamic similarity, it exists simultaneously with kinematic similarity when, for an incompressible flow, the Reynolds number of the model and full scale environment are correspondingly equal [26]. However, common scales used in wind tunnel models will not allow the compliance of the Reynolds similarity on the object, which is the case of this analysis and may cause some results discrepancy.

This lack of similarity comes from the limitations in both velocity and dimensions of the wind tunnel since it can only perform under velocities of 9 m/s. The car model was simulated for a inlet velocity of 13.9 m/s, since it was intended to be used for the rear wing optimization, meaning that the wind tunnel maximum wind speed would need to be considerably superior.

Since it was not possible to keep a dynamic similarity in the model its dimensions were picked taking into account what was found in wind tunnel literature, specially in Katz (2006) [25], where a blockage ratio less or equal to 7.5% is recommended, but not essential to obtain good results. This being said a 10% of blockage ratio was taken as the goal, in order to keep the car Reynolds number similarity as close as possible. Resulting in a 3D printed 1/4 scale model of the car that is represented in Figure 5.2, and presents the following dimensions: $0.7 \times 0.35 \times 0.3\text{m}$ (*Length x Height x Width*).

Model mounting on the wind tunnel

The third and final issue was solved through the car elevation with the use of two foams, in order to replicate its real world elevation. Other less intrusive alternatives were possible: however, since the PIV measurements can not analyze the flow under the car with the systems available, because the laser is positioned above the car and cannot be easily moved, the usage of the foams on the undertray of the car model should not significantly influence the results. Regarding the rotating wheels, when the wheels are not integrated into the body, as in single seater racing cars, the forward displacement of the separation resulting from the rotation of the wheel can be taken into consideration

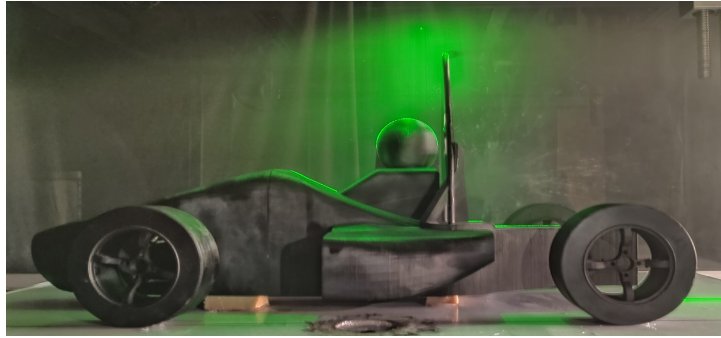


Figure 5.2: Scaled model of the car.

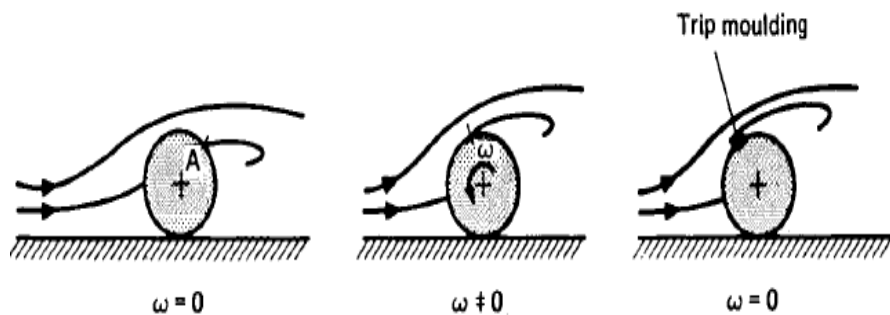


Figure 5.3: Trip moulding technique [23].

by attaching a trip moulding in the expected detachment point, "The flow pattern is then very similar to that of a rolling wheel"[23], Figure 5.3.

However, this alternative didn't reveal the expected results in Diasinos (2009) [27], in which is stated that "The flow from the wheel tread was initially separated by the addition of the gurney (tripping device), the high positive pressure gradient experienced by the flow passing over the top of a stationary wheel caused the flow over the wheel to eventually reattach" and "Similarly unsuccessful results were obtained when using regions of increased roughness on the wheel tread."

Despite this, the trip moulding alternative was meant to be tested to confirm its validity since it had an easy execution. However, this wasn't possible due to the set back in the PIV equipment, which didn't allow further tests to be made.

5.2 Flow visualization techniques

Measurements were carried out using the Particle Image Velocimetry (PIV) as a quantitative technique, and a smoke injection machine was used as a secondary qualitative option, which is based on the visualization of smoke particles trajectories when illuminated by a laser sheet. This second method didn't reveal good enough results on a visual level to be included in these analyses.

The PIV is an optical non-intrusive measurement technique capable of acquiring a quantitative velocity field at several points of a defined plane, by processing images with tracer particles moving with the flow, which allows the tracking of particles Lagrangian

evolution when going through a plane formed by a pulsating laser. This setup can be found in Figure 5.4. The PIV measurements are able to provide a velocity vector field with its components for each identified tracer particle. In addition, and with the post-processing help, it is possible to obtain not only the mean velocity magnitude but also some flow characteristic parameters, such as vorticity, at several discretized regions of the plane.

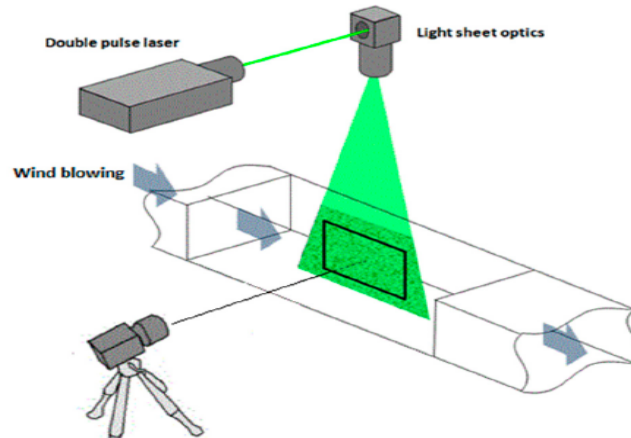


Figure 5.4: PIV used setup system [24].

For these experiments two different visualization planes were chosen that are represented in Figure 5.5. Plane 1 was positioned at the car symmetry plane, chosen with the purpose of observing both recirculating areas, in front of the pilot and behind the firewall and an overall flow performance. Plane 2 was positioned at $y=0.1$ m and was chosen with the purpose of observing the interactions of the air flow with the inside part of the wheel and the vicinity's of the side pod.

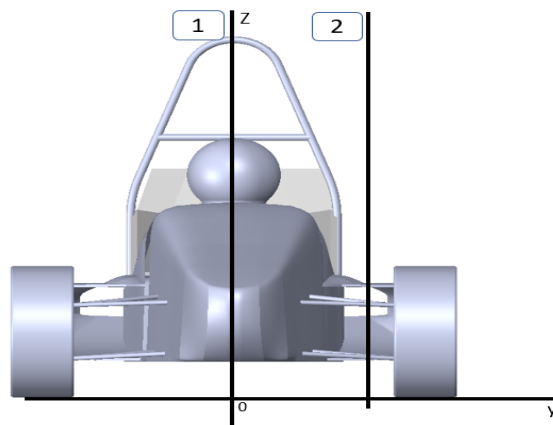


Figure 5.5: PIV section planes.

Another potential issue came to attention during the testing process, which was that the wind tunnel boundary layer could be high enough to interfere with the results, since within the boundary layer there are considerable velocity changes, and in order

to replicate the CFD simulations the air flow should be uniform when reaching the car model. The wind tunnel boundary layer height had been previously acquired through a Pitot tube and its velocity profile was made available, revealing a maximum height of 0.150 m at the center of the test section, that was where the car model was positioned. This will be taken into consideration when analyzing the PIV results for the side pod analysis, because its upper part can still be inside the wind tunnel boundary layer.

5.3 CFD results vs wind tunnel measurements

The PIV tests were initially supposed to be carried out at a wind speed of 9 m/s; however due to the referred technical problem in the PIV laser, tests were only performed for 6 m/s. Also, since the wheel rotation wasn't implemented in the wind tunnel tests a new CFD simulation was performed with no wheel rotation so that the results between them could be more fairly compared. This new simulation was performed with the full size car model, meaning that in order to keep the Reynolds number similarity the comparison between the CFD and wind tunnel results the simulation was made for an inlet velocity of 1.5 m/s.

Plane 1

A comparison between the CFD and wind tunnel results in plane 1 can be made with the aid of Figure 5.6, in which the results from the PIV measurements are available on the left-hand side and the results from the CFD simulation on the right-hand side.

The overall flow form around the car is evidently similar in both approaches, specially the recirculation formed in front of the driver and the flow near the head of the driver. However, some accuracy of the PIV results near the chassi tubes and behind the firewall was lost due to the shades created by the model, represented in pink, since the laser was positioned directly above the car. Therefore, some of the details observable on the CFD results could not be evaluated with good detail in the PIV measurements .

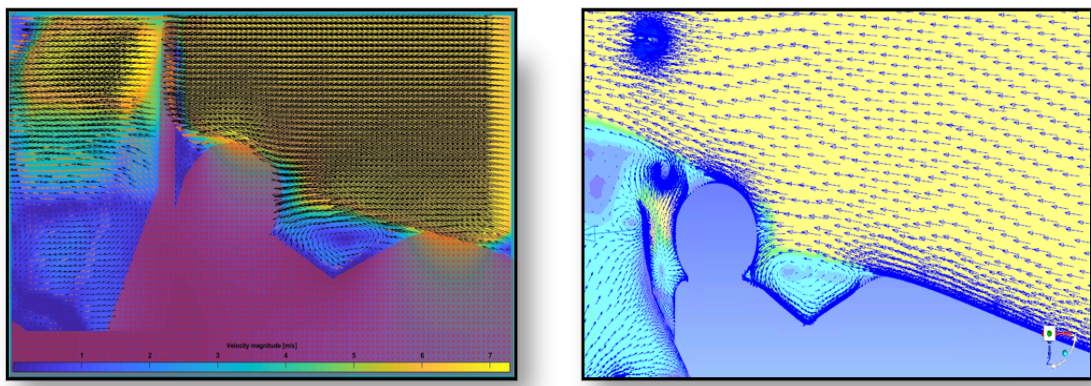


Figure 5.6: Velocity vector field for plane 1 for both wind tunnel(left) and CFD(right).

Plane 2

A comparison between the CFD and wind tunnel results in plane 2 can be made with the aid of Figure 5.7, in which the results from the PIV are available on the left-hand side and the results from the CFD simulation on the right-hand side. Since the model was opaque the flow inside the side-pod wasn't registered with the aid of the PIV, and once again some shade zones interfered with the results capture, represented in dark blue above the side-pod.

However, a gradual deceleration at the side-pod entrance is noticeable in section 1, as well as a more abrupt acceleration at the side-pod exit in section 2, and even an acceleration of the air under the end of the side-pod caused by the sectional area increase between the ground and the lower side-pod surface represented in section 3.

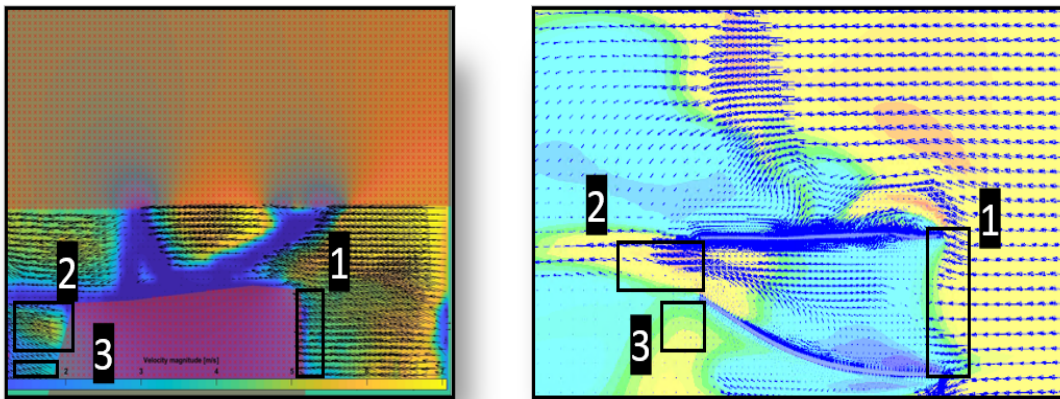


Figure 5.7: Velocity vector field for plane 2 for both wind tunnel(left) and CFD(right).

An analysis of the results provided by the CFD and wind tunnel allows to conclude that the CFD model can accurately replicate the fluid flow movements when comparing with the wind tunnel results. Although, as referred before, this only better validates the CFD simulation for lower air velocities and doesn't increase significantly the validation for the simulation used in Chapter 6, done for air velocities of 50 Km/h. However, it is always positive to have some real world corroboration to the setup used in the CFD analysis.

Chapter 6

Rear wing optimization

To fulfil the purpose of this thesis, which is to obtain the optimal multi-element rear wing for the current Formula Student Aveiro car, an optimization problem had to be outlined and solved. A wing generator was created through a MATLAB© code, while the 3D simulation of the generated wings was dealt with ANSYS Fluent, which returned its aerodynamic performance values to an optimization algorithm. The Harmony Search Algorithm was chosen as the optimization algorithm, used to reach the optimal (most performant) rear wing. The inlet of the wing optimization simulation is a velocity profile obtained from the car simulation, avoiding the simulation of the car every evaluation, sparing both time and computational effort, while keeping a good resemblance to reality. All this process can be found reported in this chapter.

6.1 Problem definition

Currently the aerodynamic performance of a car has a major role in motor sports competition and the rear wing helps primarily with braking and cornering forces for the rear tires, giving better grip through the created downforce, as stated in Section 2.2. Therefore, in this optimization problem the goal is to find a rear wing that is able to deliver high levels of downforce while keeping drag as low as possible. However, in the FSAE competition there are specific rules that limit the performance of the rear wing, which can be found in Section 2.3. The competition rules play a major role on the limitations of the generated wing designs, limiting the positioning of the wing relative to the car and consequently its overall size. From the competition rules limitations and an overall restriction from other car components, a general rear wing configuration can be found in Figures 6.1 and 6.2. From the FSAE rules and car components restrictions resulted a general rear wing with a $Wing_{span} = 1.120$ m, $Max_{Length} = 0.8$ m and $Max_{Height} = 0.35$ m, values that are used as restrictions and a base for the next steps.

However, these are not the only factors that influence and control the aerodynamic performance of a multi-element rear wing. It can be influenced by several control variables, namely:

- Car velocity
- Number of airfoils

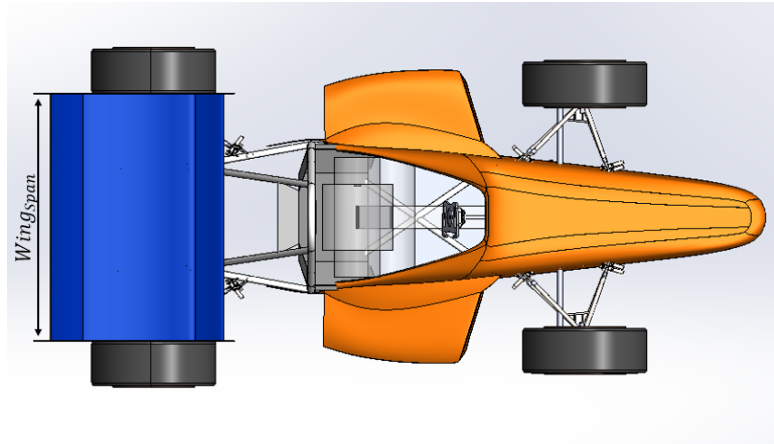


Figure 6.1: Top view of the general rear wing within the competition rules.

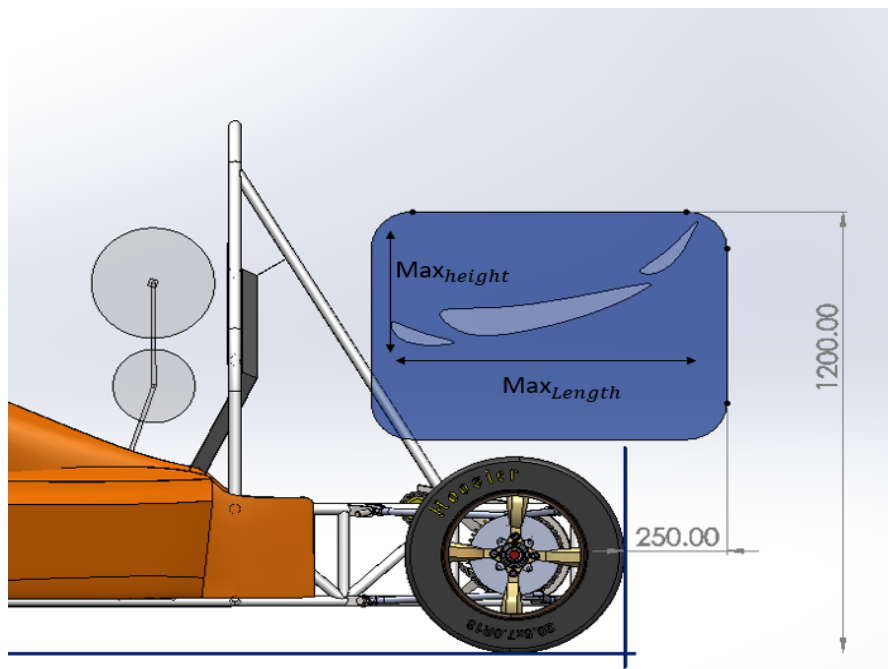


Figure 6.2: Side view of the general rear wing within the competition rules.

- Angle of attack for which airfoil
- Shape and size of the airfoils
- Relative positioning of the airfoils

Car velocity

The car velocity was kept constant along the optimization process, since simulating each rear wing iteration for a different range of speeds would be too costly both in time and computational power. The selected car velocity for the analysis was chosen from what can be found in [28, 29], where the freestream velocity of interest when designing aerodynamic package for an FSAE car is pointed to be around 13.9 m/s or 50 km/h due to the type of tests that the car will be submitted to in the competition, in which the chosen velocity is the average velocity at corners and small straights.

Number of airfoils

Most FSAE competing teams use a combination of 3 or 4 airfoils, which can be found from a generic research [30, 4, 6, 5], using both slats and flaps in order to avoid detachment of the flow for higher angles of attack, as explained in more detail in Section 2.2.3. With that information, 3 different types of configurations will be used for the rear wing optimization, which are represented in Figure 6.3.

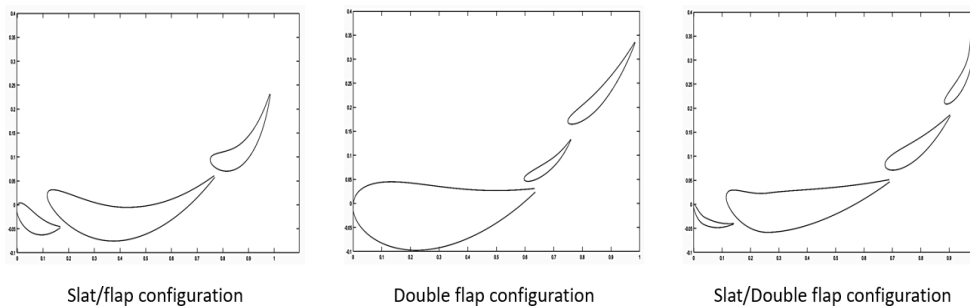


Figure 6.3: Airfoil configurations used in the optimization.

A triple flap configuration wasn't included in the optimization process, since it didn't show to be a recurrent option within the Formula Student teams.

Airfoil positioning and angles of attack

Firstly, the angles of attack for each airfoil were defined as the rotation around the corresponding leading edge. In order to define the position of each airfoil two variables were used, Gap and Overlap, and the first airfoil of the combination is always positioned at the origin. The Overlap corresponds to the superposition between two airfoils in the X-axis and the Gap corresponds to the difference, in the Y-axis, between the leading edge of one of airfoils and the trailing edge as it can be seen in Figure 6.4, where a generic multi-element wing is represented together with the positioning variables and angles of attack.

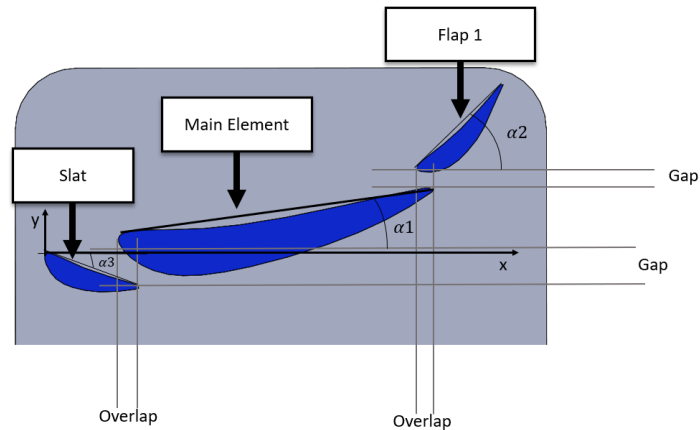


Figure 6.4: Variables that control the relative positioning of the airfoils.

Airfoil shape and size

As a means to produce different airfoil shapes the NACA 4 airfoil series was used, where through the control of 3 parameters it is possible to obtain different lift creating geometries. Since in this case the goal is to obtain downforce instead of lift forces the airfoils will be mirrored.

The 3 parameters that control the geometries can be found in Figure 6.5, and are thickness (**T**) the maximum thickness of the airfoil, maximum camber (**M**) which is the maximum height of the mean camber line that defines the curvature of the airfoil, and finally the point of maximum camber (**P**) that can be defined by the X-axis value of the point of maximum camber. All the different airfoils are initially normalized, thus meaning a chord length of 1, and the size will be defined by a scaling value.

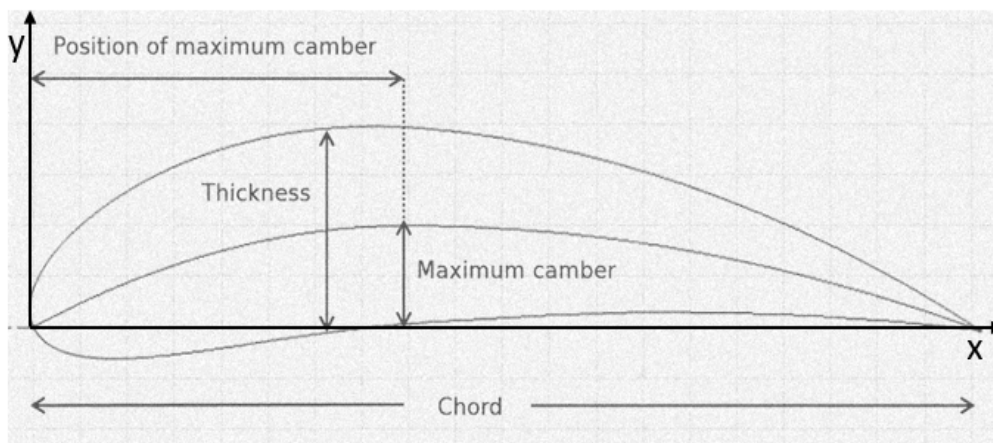


Figure 6.5: Variables that control the shape of the airfoils.

$$\begin{array}{l}
\text{Domain of the variables} \\
\text{that define the main airfoil}
\end{array}
\left[\begin{array}{l}
-5 \leq \alpha_{1,l} \leq 0, \\
40 \leq Scale_{1,l} \leq 70, \\
0.1 \leq T_{1,l} \leq 0.3, \\
0.05 \leq M_{1,l} \leq 0.15, \\
0.1 \leq P_{1,l} \leq 0.6,
\end{array} \right.$$

$$\begin{array}{l}
\text{Domain of the variables} \\
\text{that define the first flap}
\end{array}
\left[\begin{array}{l}
-40 \leq \alpha_{2,l} \leq -20, \\
15 \leq Scale_{2,l} \leq 30, \\
0.1 \leq T_{2,l} \leq 0.3, \\
0.05 \leq M_{2,l} \leq 0.2, \\
0.1 \leq P_{2,l} \leq 0.6, \\
1 \leq Overlap_{1,l} \leq 6, \\
1 \leq Gap_{1,l} \leq 4,
\end{array} \right.$$

$$\begin{array}{l}
\text{Domain of the variables} \\
\text{that define the second flap}
\end{array}
\left[\begin{array}{l}
-70 \leq \alpha_{3,l} \leq -30, \\
10 \leq Scale_{3,l} \leq 30, \\
0.1 \leq T_{3,l} \leq 0.2, \\
0.05 \leq M_{3,l} \leq 0.2, \\
0.1 \leq P_{3,l} \leq 0.6, \\
1 \leq Overlap_{2,l} \leq 6, \\
1 \leq Gap_{2,l} \leq 4,
\end{array} \right) \left. \begin{array}{l} \\ \\ \\ \\ \\ \\ \\ \end{array} \right\} \text{if } l = 2 \text{ or } l = 3$$

$$\begin{array}{l}
\text{Domain of the variables} \\
\text{that define the slat} \\
\text{in the first configuration}
\end{array}
\left[\begin{array}{l}
0 \leq \alpha_{3,l} \leq 25, \\
10 \leq Scale_{3,l} \leq 20, \\
0.1 \leq T_{3,l} \leq 0.3, \\
0.05 \leq M_{3,l} \leq 0.2, \\
0.1 \leq P_{3,l} \leq 0.6, \\
2 \leq Overlap_{2,l} \leq 10, \\
2 \leq Gap_{2,l} \leq 8,
\end{array} \right) \left. \begin{array}{l} \\ \\ \\ \\ \\ \\ \\ \end{array} \right\} \text{if } l = 1$$

$$\begin{array}{l}
\text{Domain of the variables} \\
\text{that define the slat} \\
\text{in the third configuration}
\end{array}
\left[\begin{array}{l}
0 \leq \alpha_{4,3} \leq 25, \\
10 \leq Scale_{4,3} \leq 20, \\
0.1 \leq T_{4,3} \leq 0.3, \\
0.05 \leq M_{4,3} \leq 0.2, \\
0.1 \leq P_{4,3} \leq 0.6, \\
2 \leq Overlap_{3,3} \leq 10 \text{ and} \\
2 \leq Gap_{3,3} \leq 8.
\end{array} \right.$$

In the multi objective function $P(S_1, S_2)$, β is the member responsible for the relevance control of each objective function, and r is the member responsible for the magnitude equalization of both objective functions, S_1 and S_2 . In other words, S_1 and S_2 have different levels of relevance for example, as the vehicle will be moving at considerably low velocities the donwforce component will play a major role in the car performance

when compared with the drag force, so the function S_1 will be given greater importance in the multi objective function $P(S_1, S_2)$. In order to make this possible S_1 and S_2 have to be equalized first, for example if S_1 is usually 10 times greater than S_2 , then r will be set to 10.

It is also important to state that this optimization problem is of the black-box type, meaning that the function F is dependent on auxiliary programs to obtain both C_l and C_d values. In this case the auxiliary programs used for that purpose were MATLAB© and ANSYS Fluent. The variables $X_{i,j}$ and $Y_{i,j}$ represent the airfoil coordinates, N is the number of points from which the airfoil will be created and j the discrete variable that represents the airfoil number and can vary between 1 and m , being m equal to the maximum number of airfoils for each type of configuration.

The coordinates $X_{i,j}$ can be obtained through the positioning variables $\alpha_{j,l}$, $Scale_{j,l}$ and $Overlap_{k,l}$, which were defined in Section 6.1 and function g_1 which initially generates values of $X_{i,j}$ outlined by a linspace and then applies translations, rotations and a scaling to its values in accordance with the positioning variables values.

Similarly, the coordinates $Y_{i,j}$ can also be defined by the shape variables $T_{j,l}$, $P_{j,l}$, and $M_{j,l}$, which were explained in Section 6.1, the positioning variables $\alpha_{j,l}$, $Scale_{j,l}$ and $Gap_{k,l}$, and finally the coordinates $X_{i,j}$. The airfoil coordinates $Y_{i,j}$ define the airfoil shape that can be plotted by function g_2 which is a variation of the NACA 4 airfoil shape functions presented in Figure 6.8. Variable k represents the number of the gap/overlap and l is the airfoil configuration number which can vary between 1 and c , being c defined as 3 for this optimization problem. Figure 6.6 helps for a better clarification of the numeration and organization of the stated variables.

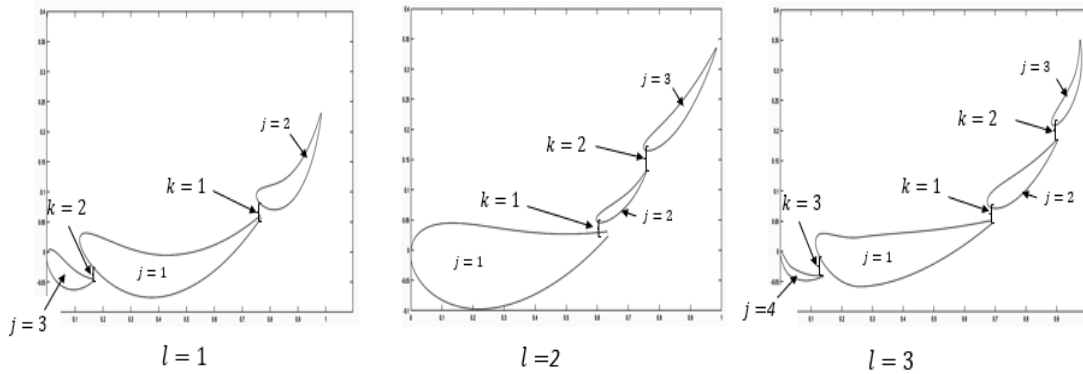


Figure 6.6: Airfoil configurations and relative organization.

It is also important to refer that in the MATLAB© optimization code the type of configuration l is defined by two binary variables $slat$, $flap_2$. Their values are defined by a rand feature that generates a random number with uniform distribution from [0,1] and if $rand > 0.5$ then the binary variables are equal to 1. Therefore, the configuration $l = 1$ happens when $slat = 1$ and $flap_2 = 0$, $l = 2$ happens when $slat = 0$ and $flap_2 = 1$, and finally $l = 3$ happens when $slat = 1$ and $flap_2 = 1$.

The objective function $P(S_1, S_2)$ in Equation (6.1) is then subjected to the inequality constraints that can be related to the test functions f_1 , f_2 and f_3 present in Section 6.3.2. Equations (6.2), (6.3) and (6.4) can be associated to f_1 , and its purpose is to keep the generated rear wing geometries within its length and height limits, while Equation (6.5)

can be associated to f_2 and its purpose is to keep the airfoil shapes viable, since during the development process it was observed that airfoil shapes which didn't respect Equation (6.5) would cause problems in the mesh phase and produce non manufacturable airfoils. In Equation (6.6), g_2, j means that the function g_2 depends on variables with index j which defines the airfoil number. This equation can be associated to f_3 in which airfoil intersections will be tested, and since the function g_2 defines the shape and position of each airfoil the function defining the airfoil, g_2, j , will always be different from the next one, $g_2, j + 1$.

The objective function $P(S_1, S_2)$ is still subjected to domain constraints, that were added to the formulation with the purpose of restricting the search domain and to approximate the solutions to the optimum result. Some of the variables were attributed a domain based on the testing done in the development phase of the project, for example the shape defining variables $T_{j,l}$, $P_{j,l}$ and $M_{j,l}$. However, for some variables it was possible to find some literature that presented a range of values among which it can be usually found the optimum performance of a multi element rear wing for a one-seater car,[30, 8]. For example from McBeath (2015) [8] it was possible to gather the range of optimum values for the $\alpha_{j,l}$, in degrees, and $Scale_{j,l}$, $Overlap_{k,l}$ and $Gap_{k,l}$ in percentage values for both flaps. On the contrary, no literature was found containing information about slat positioning, so a larger range of values was chosen.

With the purpose of adjusting the domains to the problem at hand some modifications were made to what was found in the literature. For example, the minimum scale of both flaps was lowered so that higher angles of attack were possible despite the limited max_{height} , and the maximum angle of attack of Flap 1 was also increased since it would be the only flap in configuration $l = 1$, thus a higher angle of attack might be beneficial to its performance.

6.3 Evaluation process

A shape optimization exercise requires the development and coupling of several elements in an automatic chain. A shape modeling system which converts the design variables into a shape (1-2), a grid generation program that generates a surface grid and a volume grid and a CFD solver (3), and finally an optimizer (4). These can be found in Figure 6.7, and each one will then be analyzed in the following sections.

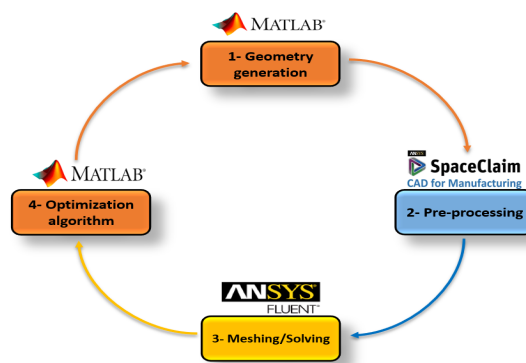


Figure 6.7: Diagram of the evaluation process.

6.3.1 Geometry generation

Firstly, the evaluation process goes through a geometry generation procedure, where the control variables generated by the optimization algorithm are used to define the new rear wing geometry. This was done with the help of MATLAB©, in which a script was coded to create a text file containing the coordinates $((X_{i,j}, Y_{i,j}) \cdot max_{length})$ of the rear wing configuration. The coordinates for each airfoil are initially obtained through the NACA 4 variables and the shape functions that can be found in Figure 6.8.

	Front ($0 \leq x < p$)	Back ($p \leq x \leq 1$)
Camber	$y_c = \frac{M}{p^2} (2Px - x^2)$	$y_c = \frac{M}{(1-p)^2} (1 - 2P + 2Px - x^2)$
Gradient	$\frac{dy_c}{dx} = \frac{2M}{p^2} (P - x)$	$\frac{dy_c}{dx} = \frac{2M}{(1-p)^2} (P - x)$

The thickness distribution is given by the equation:

Where:

$$y_t = \frac{T}{0.2} (a_0 x^{0.5} + a_1 x + a_2 x^2 + a_3 x^3 + a_4 x^4)$$

$a_0 = 0.2969$	$a_1 = -0.126$	$a_2 = -0.3516$	$a_3 = 0.2843$
$a_4 = -0.1015$ or -0.1036 for a closed trailing edge			

$$\theta = \text{atan} \left(\frac{dy_c}{dx} \right)$$

Upper Surface	$x_u = x_c - y_t \sin(\theta)$	$y_u = y_c + y_t \cos(\theta)$
Lower Surface	$x_l = x_c + y_t \sin(\theta)$	$y_l = y_c - y_t \cos(\theta)$

Figure 6.8: NACA 4 series shape functions (<http://airfoiltools.com/airfoil/naca4digit>).

The shape functions were inverted and the trailing edge was kept in an open configuration as it is possible to see highlighted in Figure 6.9, instead of the closed trailing edge presented in Figure 6.5. This trailing edge configuration was chosen since it considerably improved the quality of mesh creating process, which will be analyzed in detail in Section 6.3.2.

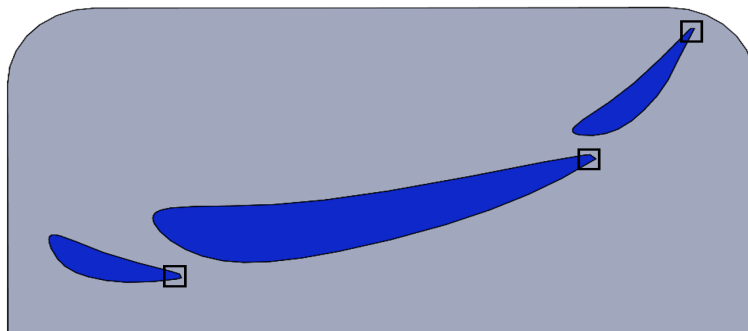


Figure 6.9: Open trailing edge representation of a created geometry.

After the definition of the airfoil geometry, the MATLAB© script proceeds with the scaling of the airfoil, followed by a rotation and translation, where in the end a similar geometry to what can be found in Figure 6.3 is expected. The wing geometry is normalized, meaning that all the lengths of the wing geometry will be within the [0,1] interval, and only after that it will be scaled to the real world case, in this case multiplying the geometry coordinates by Max_{length} . All the wing creation operations are conducted by the variables present in Equation 6.1, which are controlled by the optimization algorithm.

After the rear wing geometry is finished it will be tested by three different functions:

- f_1 - Checks if the geometry is within the length and height limits
- f_2 - Checks if the airfoils have a viable shape
- f_3 - Checks if the airfoils intersect each other

In case the generated geometry doesn't go through all these tests successfully, new control variables will be asked to the optimization code until the geometry successfully passes all functions. Hereupon, when the airfoil geometry passes the restrictive function it is ready for the next step of the evaluation process, which will receive the created text file with the rear wing geometry, Figure 6.10.

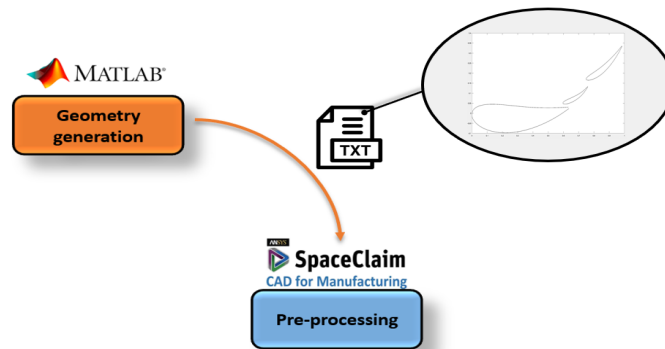


Figure 6.10: Transition from the generated geometry to pre-processing.

6.3.2 Pre-processing

The pre-processing of the geometry was done with ANSYS SapceClaim, where 3 script files were created each one for a different airfoil configuration, like the ones presented in Figure 6.3. The scripts were created through ANSYS SapceClaim scripting functionality, and they execute a set of previously chosen actions. The first is the import of the airfoil geometries present in the (.txt) type file, followed by an extrude of the airfoil faces. The rear wing for the optimization process has a $Wing_{span}$ of 1.120 m. Since only half of the wing needs to be tested, due to the symmetry of both the rear wing and car relative to the longitudinal mid plane, the extrude will create a rear wing with 0.560 m span.

As mentioned in Section 2.2.3, an end-plate is frequently used in the rear wing layout in order to mitigate wing tip vortices, increasing the lift induced drag component. So

a simple end-plate was created and used along with the various rear wing iterations. Despite the end-plate not being targeted for this optimization, it is a possibility for future work, since it may have a great impact on the rear wing performance. The result of the first steps of the scripting file can be found represented in Figure 6.11.

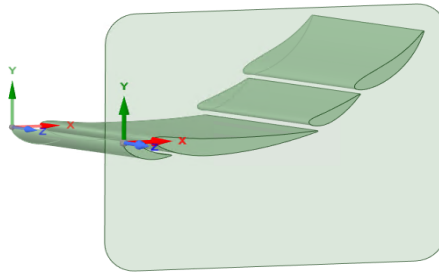


Figure 6.11: 3D rear wing with its end-plate.

The relative positioning of the airfoils and end-plate has to be taken into account, so in order to keep them independent from the type of wing configuration and airfoil shape, the first point of the first wing of each configuration will always be positioned in the origin, as it can be seen in Figure 6.11.

Ideally, the distance between the highest point of the wing configuration and the top of the end-plate would always be constant, since it would result in the wing being at its highest possible point, meaning that it would receive the greatest amount of undisturbed airflow, from what was concluded in Section 4.4.3. However, since the wing configurations will have different heights, for this to be possible the script file from ANSYS Spaceclaim had to be edited in each evaluation. When trying to edit this file it kept getting corrupted and no alternative was found for this problem, so the first alternative described above was used.

After both wing and end-plate geometries are created the enclosure and body of influence of the simulation will be prepared, Figure 6.12.

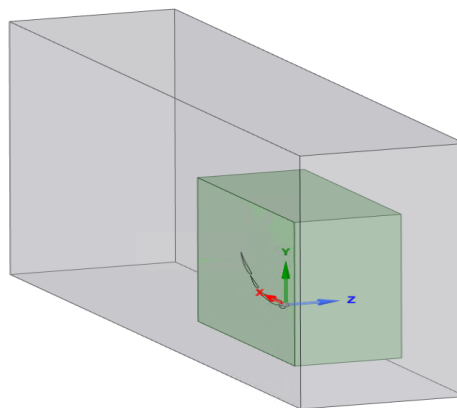


Figure 6.12: Simulation enclosure and body of influence

Similarly to what was done for the car simulation in Chapter 4, the size of both enclosure and body of influence suffered various changes during the testing process, reaching a final size of 5.1x2.2x1.25m and 1.7x1.25x0.75m (*Length x Height x Width*) correspondingly. The sizes of both enclosure and body of influence resulted from a balancing between simulation accuracy and time, where the minimum size of the enclosure that allowed flow restoration was used.

Finally, the script also included a named selections part, where surfaces were grouped in order to apply the boundary conditions and different mesh sizes to the wing surfaces in the following simulation steps, Figure 6.13.

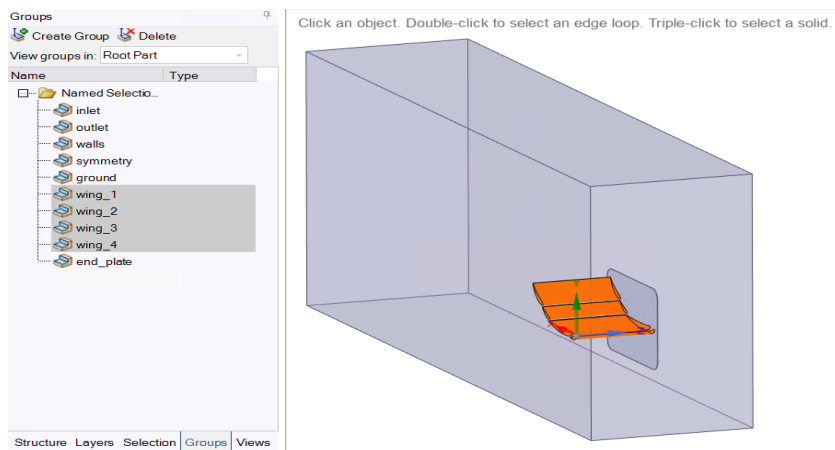


Figure 6.13: Named selections created for the mesh refinement.

Concluded the pre-processing a document of the type (.scdoc) containing both the wing geometry, end-plate and enclosure will be sent to the meshing/solving stage, Figure 6.14.

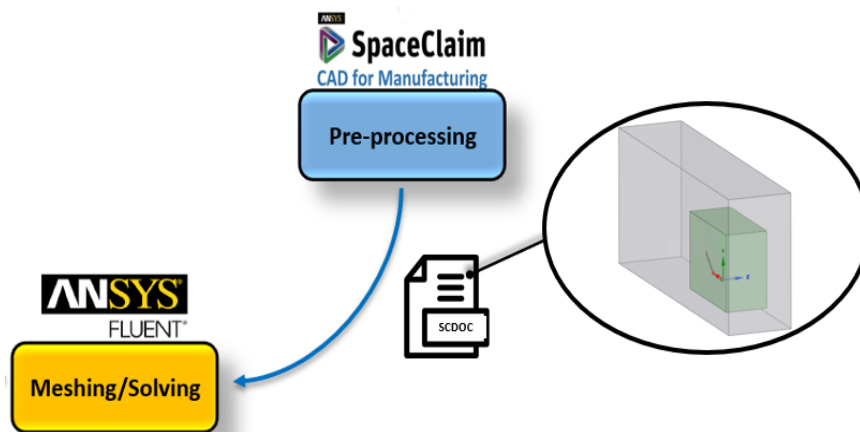


Figure 6.14: Transition from the generated geometry to pre-processing.

6.3.3 Meshing/Solving

Mesh

The mesh creation and the CFD setup was done through ANSYS Fluent 19, and in order to automate the mesh and setup creation, just as in the previous sections, a script containing all necessary steps was created. The script was made in a (.txt) type file and contains different variables that can be automatically modified during the optimization process.

In resemblance with the meshing process described in Section 4.2, a surface mesh is created and from that a poly-hexcore volume mesh is computed. For the surface mesh both curvature and proximity features were used and applied to the named selection created in the pre-processing step, so that the mesh would recreate the wing geometry accurately, Figure 6.15. As stated in Section 6.3.2, an open trailing edge configuration was chosen for the airfoil profiles and it was done with the purpose of increasing the quality of the mesh near the trailing edge. The open configuration revealed a better meshing performance since it represents the trailing edge with various number of edges, allowing the use of the edge proximity functionality and that way enabling a better local refinement. On the other hand, with a closed configuration the trailing edge is represented by a fillet with small radius and no edges. In spite of the presence of the curvature feature, which helps with the definition of high curvature geometries, for a small radius, like the one in the open configuration, the mesh would need to be extremely refined and even then from what was possible to conclude with some testing it wasn't able to always replicate the geometries.

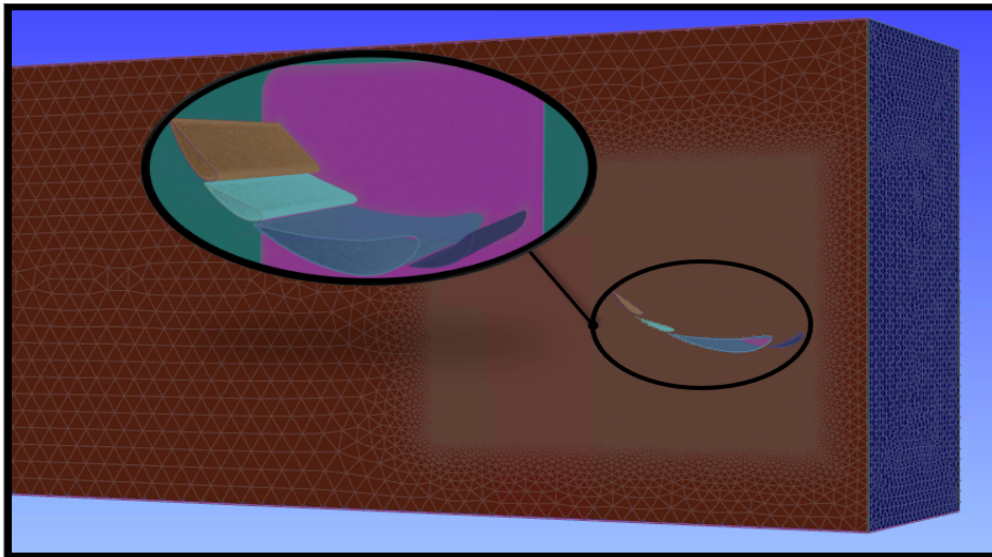


Figure 6.15: Surface mesh for one of the generated wing geometries.

It is also important to mention that the inlet surface, represented in dark blue in Figure 6.15, was hard meshed so that every element of the inlet would have the same size and would not be affected by the other surfaces meshes, what would prove to be useful when importing the velocity profiles from the car simulation.

For the volume mesh, similarly to what was used for the car simulation a poly-

hexcore was chosen and 10 prism layers were applied to all the airfoils, in order to better replicate the wing boundary layers, which can be seen in Figure 6.16. The first layer of the boundary layer refinement was sized through the same process described in Section 4.4.1, aiming for an y^+ equal to 1.

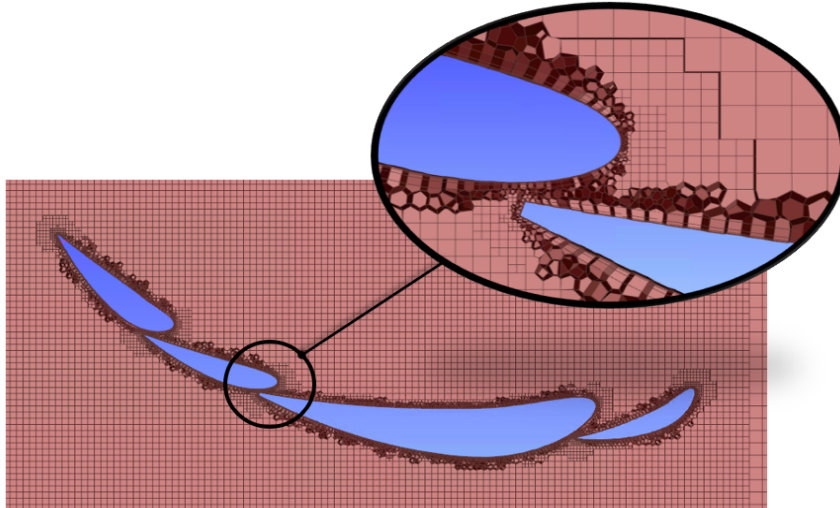


Figure 6.16: Volume mesh for one of the generated wing geometries.

Setup

The ANSYS Fluent setup is executed through a similar script file as the one used to create a mesh, the turbulence model used for the rear wing optimization was the $k - \omega$ SST model, which revealed to be the most used turbulence model in wing simulations. The boundary conditions used for the rear wing simulations are summarized in Table 6.1.

Table 6.1: Boundary conditions.

Named Selection	Boundary Condition
All wing faces	No-Slip Wall
Ground and Enclosure walls	Moving Wall at V_{in} (m/s)
Inlet	V_x (m/s) V_y (m/s) V_z (m/s)
Outlet	0 Gauge Pressure Average Pressure
Symmetry	Symmetry Condition

From Table 6.1 it is possible to observe that the inlet is defined by the three velocity components, these obtained from an adaptation of the car simulation, and its capture

process will now be explained in detail, temporarily stopping the evaluation process explanation.

Firstly a new car simulation was created, similar to the one present in Chapter 4: however, in order to create agreement between the car and rear wing simulations, the new car simulation enclosure size was lowered to 8.3x2.2x1.5m (*Length x Height x Width*), Figure 6.17, keeping both width and height in agreement with the rear wing enclosure described in Section 6.3.2.

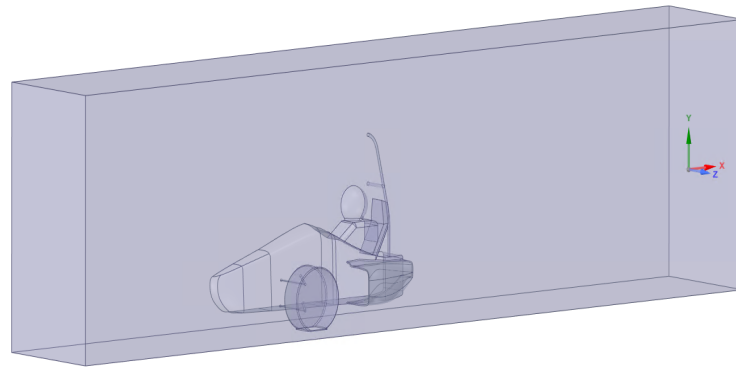


Figure 6.17: New car enclosure for the rear wing inlet velocity profile values.

The mesh and setup parameters used for the adapted car simulation are the same as the ones used for the most accurate simulation presented in Section 4.4.2. Since the enclosure size was lowered significantly the simulation results could be corrupted; however, after a fast comparison between the car simulations for the different enclosures, the velocity profile in the focus area kept its properties from one simulation to another. Since the new simulation revealed good results it was possible to proceed with the velocity profile collecting. In order to make this possible a plane was created and can be found represented with black color in Figure 6.18.

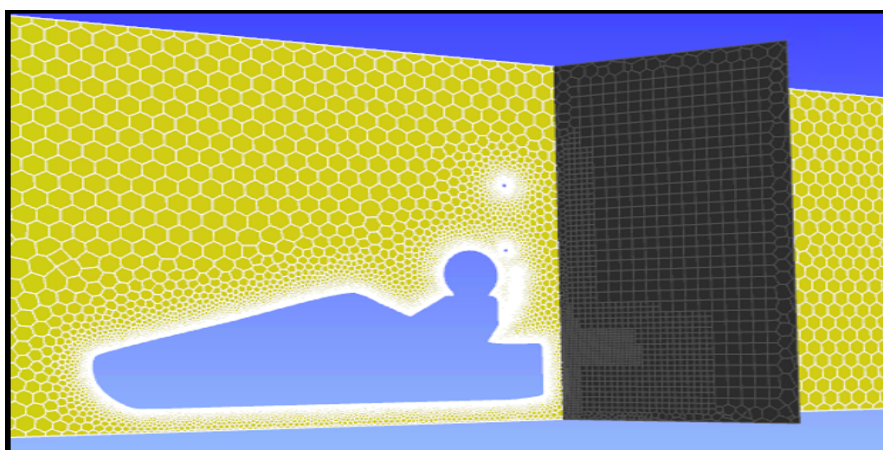


Figure 6.18: Plane for the capture of the inlet velocity profile values.

The placement of the velocity profile capture plane suffered a number of changes during the development process, since its placement may affect both car and rear wing

simulations. In the case of the car simulation the plane had to be behind the car geometry otherwise the plane would not be completely filled, since the car geometry would penetrate it. On the other hand, if the plane was pushed further away from the car it would be too close to the rear wing, and the inlet velocity profile for the rear wing simulation would be affected by the disruption caused by the rear wing itself. The final plane was positioned at a distance of 250 mm from the foremost point of the wing, which, in order to maintain conformity between the simulations, was the defined distance between the inlet velocity plane and the wing in the rear wing simulations.

Figures 6.19 and 6.20 represent the velocity components from the plane in the car simulation and the velocity components in the rear wing simulation inlet after its computation, respectively. It can be concluded that the suggested simplification of the car/rear wing simulation has a good level of accuracy since the velocity profiles can be replicated with a high level of resemblance both for minimum and maximum velocity values and in a qualitative velocity distribution standpoint.

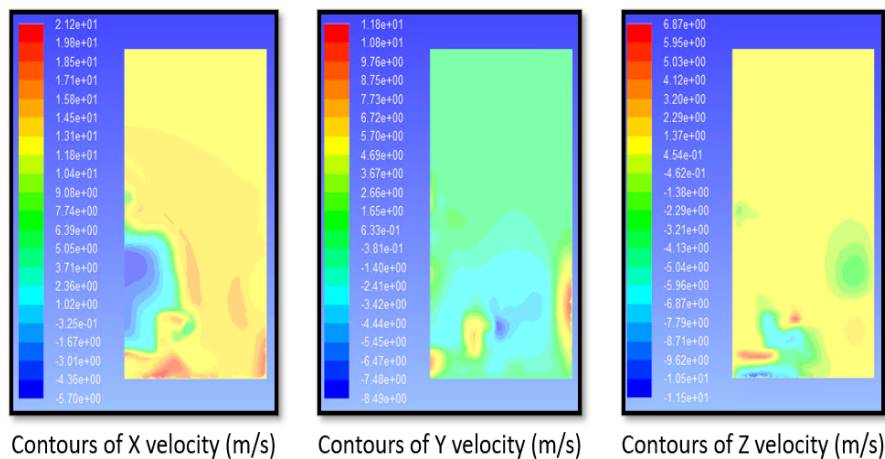


Figure 6.19: Velocity profiles captured from the plane created for the car simulation.

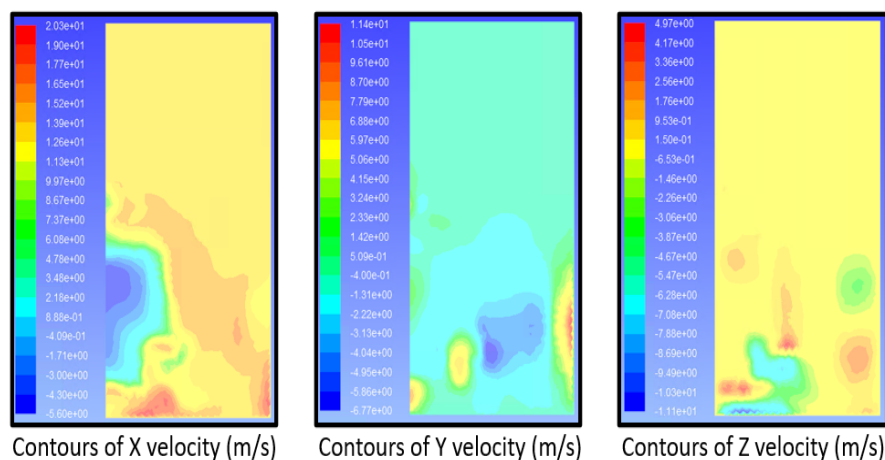


Figure 6.20: Velocity profiles from the rear wing inlet after a simulation.

Concluded the velocity inlet explanation, it is now possible to continue the evaluation process description, where the setup section is also responsible for the calculation of the lift and drag non-dimensional coefficients, C_d and C_l , and for that the reference values stated in Table 6.2 need to be defined. Since within the geometries generated through the optimization process the frontal area of the rear wing will change, the frontal area is calculated in the geometry generation process and that information is updated in ANSYS Fluent at every evaluation. The remaining variables are kept constant through all the evaluation process.

Table 6.2: Fluid flow reference values.

Reference Values for ANSYS Fluent				
<i>Projected Frontal Area (m²)</i>	ρ (kg m ⁻³)	μ (m s ⁻³)	U (m s ⁻¹)	<i>Length(m)</i>
A_{Front}	1,225	$1,7894 \cdot 10^{-5}$	13.9	0.8

With the velocity inlet and reference values defined, the only things left to create a fully automated rear wing simulation are the implementation of a stop criterion and the recording of the aerodynamic forces applied to the wing. For that, force reports were created, responsible for capturing C_l and C_d values within the wing and end-plate surfaces for every iteration of the simulation. The values from the force reports are then used as stop criterion for the simulation, which was initially set as an oscillation lower than to 1% on both C_d and C_l from the previous 30 iterations. The 1% oscillation on C_l and C_d results on a maximum variation of around 0.5 N on both lift and drag forces, what is negligible for the type of evaluation intended with this optimization. In case the stop criterion couldn't be achieved, a maximum number of iterations for the simulation was defined and if at the end the stop criterion wasn't met then both C_d and C_l would be forced to a value of 0.404 in the MATLAB© optimization code. The 0.404 value is associated with an error, and meaning that the simulation wasn't accurate enough to be considered in the optimization process.

In the end, in order to optimize the mesh and search for more accurate results, a mesh convergence study was conducted for an arbitrary wing shape. Through the mesh convergence testing of five different meshes, it was possible to conclude that the mesh with 2.19 million cells offered a good quality of results while keeping the run time within acceptable levels, and was chosen for the first run of the optimization process. This was concluded from the information available in Figure 6.21, where the C_l values for the different meshes are represented in red and the C_d values in blue, and in the second graph the run time for the evaluation of the wing can be found, which has a major role in the optimization process since this process will be repeated hundreds of times.

Concluded the Meshing/Solving process a document of the type (.out) containing the values of both C_l and C_d will be sent to the optimization algorithm and used to generate a more optimized rear wing geometry, Figure 6.22.

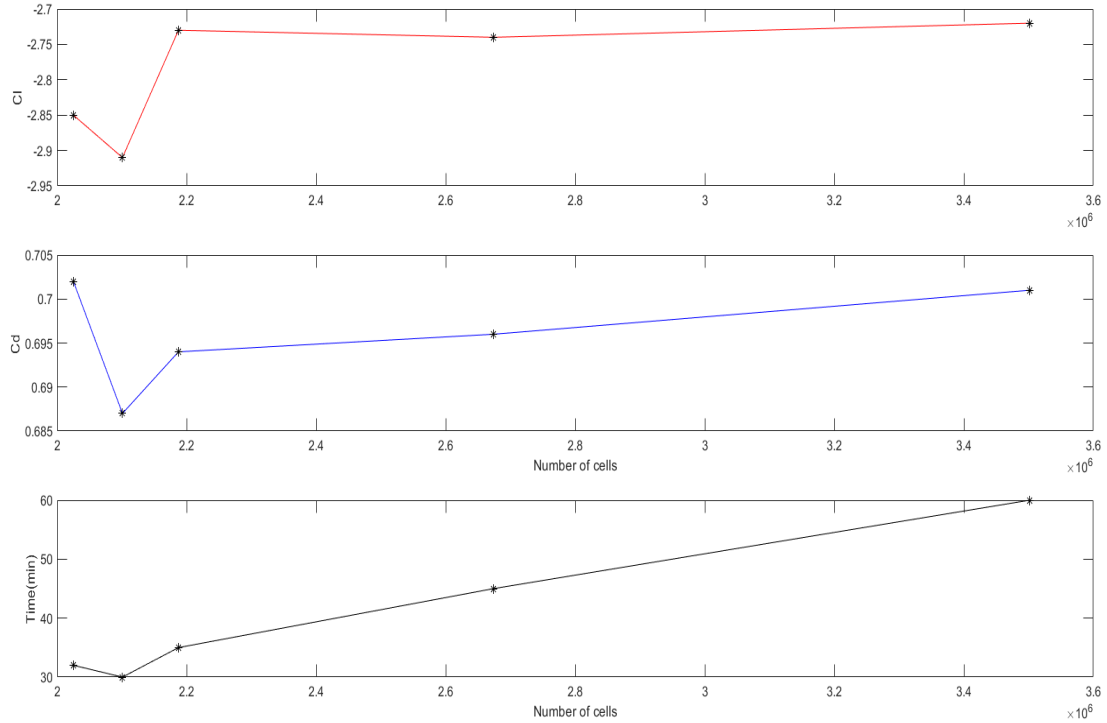


Figure 6.21: C_l , C_d and run time of the simulations for the different tested meshes.

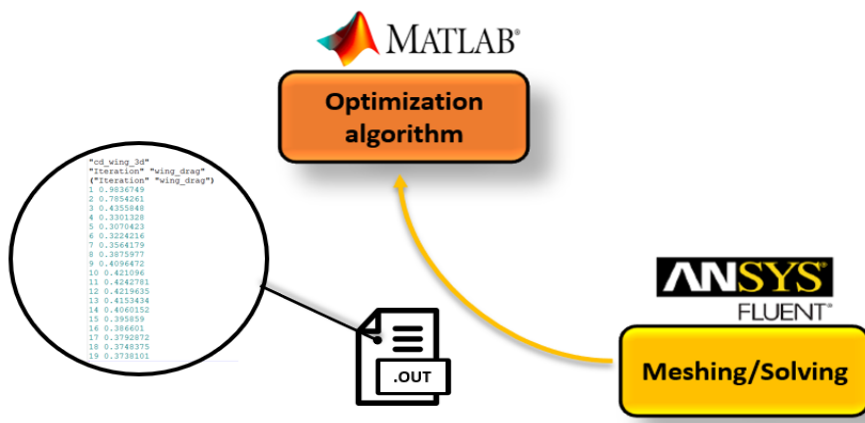


Figure 6.22: Transition from the simulation to the optimization code.

6.3.4 Optimization algorithm

With the values from the simulation the optimization algorithm will generate new control variables that gradually create better performing rear wing geometries. For the optimization algorithm there are a number of viable meta-heuristic options to solve this optimization problem. However, in a previous analysis to a similar problem [31], carried out in the context of a non-linear optimization course in 2021, some testing was already done for a single element rear wing, in which its shape and angle were changed and its simulations executed using Xfoil. In that analysis an Harmony Search Algorithm (HSA) adapted from [32] was used and revealed good results. For that reason the HSA was also chosen as the optimization algorithm for the problem at hand.

This meta-heuristic algorithm is based on musical principles, and in the harmony improvisation process of musicians in finding a pleasing harmony. Through parameters of random character it also has the capability of searching both local optimum and global optimum of non-linear problems.

When a musician wants to tune the pitch of its instrument and plays a note there are three possible ways to do that, these options being the main body rules of HSA:

1. A note can be played randomly from a defined range.
2. A note stored in memory can be played.
3. A note in the vicinity's of a note already in memory can be played.

Given a small introduction of the HSA foundations, a more detailed approach will be taken in the following paragraphs, where the full process of the HSA will be explained. The HSA starts by randomly generating an Harmony memory (HM), this memory can have a different number of harmonies stored and its size can be controlled by the user, represented in Figure 6.24, where N is the number of stored harmonies, d the number of note per harmony, and f the value from the objective function.

Then, a new harmony is improvised in each iteration, and each harmony will be constituted by x_j , or notes, with $j = 1, \dots, d$, represented in Figure 6.23. For the rear wing optimization problem $d = 28$ since those are the number of notes needed to form the wing shapes. So, a note in this case can be the angle of the first flap in configuration 2 ($\alpha_{2,2}$). The 28 notes consist of the 26 variables that define the shape and position of the airfoil and of the 2 variables *slat* and *flap₂* that control the type of airfoil configuration.

The new harmony can be a random value within the domain, a partial copy of an harmony stored in the HM, and even a tuning of an harmony present in the HM. These possibilities are controlled with the help of the following parameters: harmony memory considering rate (*HMCR*), pitch adjusting rate (*PAR*) and bandwidth of generation (*bw*), all these parameters varying between 0 and 1. Therefore, *HMCR* is the probability of generating a random note, *PAR* defines the probability of tuning a note taken from the HM and *bw* is the bandwidth that controls the intensity of the tuning. The pitching adjustment parameters *PAR* and *bw* are used to escape from local optima, in which small values of *PAR* lead to a weak pitch adjustment and large values of *PAR* lead to a rich pitch adjustment.

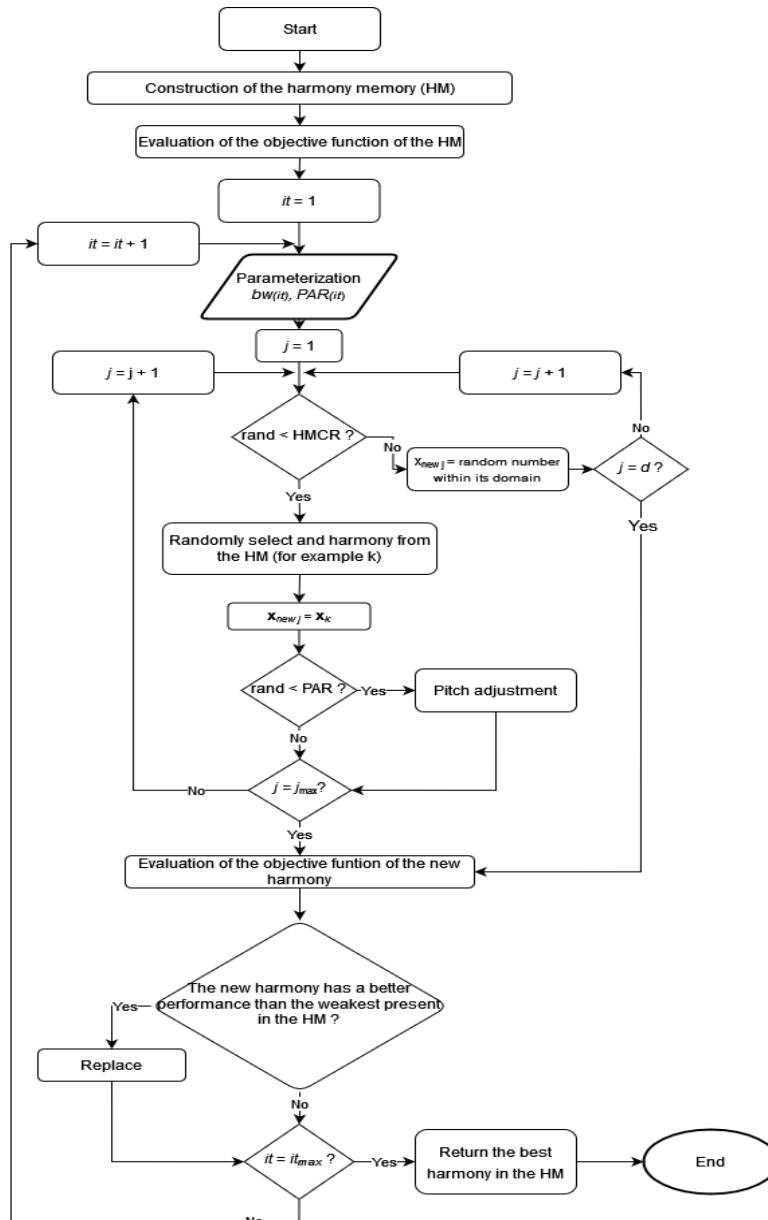


Figure 6.23: HSA flowchart.

	x_1	x_2	...	x_d	f
Harmony 1	$x_{1,1}$	$x_{1,2}$...	$x_{1,d}$	f_1
Harmony 2	$x_{2,1}$	$x_{2,2}$...	$x_{2,d}$	f_2
⋮	⋮	⋮		⋮	⋮
Harmony N	$x_{N,1}$	$x_{N,2}$...	$x_{N,d}$	f_N

Figure 6.24: Harmony memory structure of the HSA [32].

In order to respect the x_j domain during the pitch adjustments, the pitch was corrected through the following equation:

$$x_{new,j} = x_{new,j} + rand(-bw(-x_{min} + x_{new,j}), bw(x_{max} - x_{new,j})), \quad (6.7)$$

$$x_{new,j} \in [x_{min}, x_{max}]$$

where $x_{new,j}$ is a new note of the variable j with domain $[x_{min}, x_{max}]$. This was an adaptation of the pitch adjustment equation presented in Askarzadeh and Rashedi (2017) [32], and it was necessary since for notes with values outside of the domain the simulation could crash and corrupt the optimization process.

Previous investigations on the HSA performance have shown that it has a good ability in exploration and can discover potential solutions quickly.[32] However, the local and more detailed search ability of the HSA is weak so it just stabilizes its value in later iterations of the algorithm. Therefore, in order to avoid that, one of the most popular variants of the HSA, made by Mahdavi et al. in 2007 [33] was used . Based on the suggestions made by [33], time-varying values for PAR and bw are proposed, the value of PAR increasing linearly during the iterations as

$$PAR(it) = PAR_{min} + \frac{PAR_{max} - PAR_{min}}{it_{max}} it, \quad (6.8)$$

where $PAR(it)$ is the PAR value at iteration it , it_{max} is the maximum number of iterations, PAR_{min} is the minimum PAR value and PAR_{max} is the maximum PAR value.

The value of bw decreases non linearly during the iterations, according to [33], and can be equated through the following exponential function,

$$bw(it) = bw_{max} \times e^{(Ln(\frac{bw_{min}}{bw_{max}}) \frac{it}{it_{max}})}, \quad (6.9)$$

where bw_{max} and bw_{min} are the maximum bandwidth and minimum bandwidth, respectively.

After the completion of the new harmony, it will be subjected to all the processes present in Figure 6.7, which were described in detail previously, evaluated through the objective function and finally tested to examine if it will be included in the HM.

This process will be repeated until the stop criterion is met, and then the best harmony stored in the HM will be returned as the optimum solution for the problem. The stop criterion was defined as $it = it_{max}$; however, ideally, a convergence criterion

based on the objective function values would be used, although due to the time available for the completion of the thesis it wasn't possible to gain enough sensitivity in the subject to define a convergence criterion.

6.4 Optimization improvement runs

In order to improve the optimization parameters and objective function to what was intended for the rear wing, it was subjected to 4 test runs. All the improvement runs were executed for a maximum of 80 harmony evaluations and an HM composed of 10 harmonies, these being initially obtained for $HMCR = 0.7$, $PAR_{min} = 0.25$, $PAR_{max} = 0.8$, $bw_{min} = 0.01$ and $bw_{max} = 0.5$, which were defined from the previous work done in Novais (2021) [31].

These values were prescribed so that the optimization process wasn't excessively time consuming, while giving a sufficient number of evaluations so that the optimization algorithm could deliver interesting useful results.

In order to evaluate the results provided from the optimization code two types of representations were chosen. In Figure 6.25 and similar representations, a evolution of the HM values can be found together with a representation of the best wing shapes evolution, for each of the 3 different wing configurations, the final best configuration is represented in blue and the 4 previous best values in red, the worst values present are more transparent and the best are more opaque. In Figure 6.26 and similar representations, contain a table from MATLAB© which has a partial representation of the final harmonies in the HM, focusing on the objective function and simulation results, and where alpha is the overall angle of attack of all wings and f is the value of the objective function.

6.4.1 Test run with $S_1 = C_l$

The coefficients C_l and C_d are recurrently used to define the aerodynamic performance wings. However, these non-dimensional coefficients, defined in Equations (6.10) and (6.11), can define the performance when the reference area (A), air density (ρ) and velocity (V) are kept constant along the analysis.

$$C_l = \frac{Lift}{\frac{1}{2}\rho V^2 A} \quad (6.10)$$

$$C_d = \frac{Drag}{\frac{1}{2}\rho V^2 A} \quad (6.11)$$

Despite both speed and density being kept constant during the optimization process, the reference area will not be equal for every rear wing generated and will be updated for every new wing shape, meaning that possibly C_l and C_d are not the ideal variables to evaluate the rear wings performance. For this reason the optimization code described in this chapter was tested, with $r = 1$ and $\beta = 0.75$. β was set to 0.75 in order give a larger importance to C_l over the C_d values, since the defined objective of this optimization problem, defined in Section 6.1, was to maximize downforce while keeping drag under control. The whole optimization test run took 47 hours and had an average evaluation time of 31 minutes, the results evolution and final HM composition can be found in

Figures 6.25, 6.26 and 6.27 . For this test run Figure 6.27 was added to the remaining in order to easily compare the best value evolution between C_l and $Lift$.

From these results, 3 main conclusions were withdrawn:

- For the best value evolution, in Figure 6.27, the values of C_l and $Lift$ follow the same behaviour, this meaning that when C_l increases the $Lift$ follows the same path. However, from the final HM, present in Figure 6.26, it is possible to conclude that the highest C_l values aren't necessarily connected with the highest $Lift$ values. Therefore, for the next test the objective function S_1 will be $S_1 = Lift$, since the main goal is to produce the most amount of negative $Lift$ (Downforce).
- From the HM in Figure 6.26 it was possible to conclude that the $Lift$ values are usually 4 times higher than the $\frac{C_l}{C_d}$, so in order to maintain the two variables balanced r should be changed to $r = 4$ for the next test run. It was also possible to conclude that the objective function was prioritizing low overall angles of attack ($alpha$) and high $\frac{C_l}{C_d}$, over the high $Lift$ values intended for this optimization problem.
- Finally, the HM ended with only one type of configuration, the one slat one flap configuration, this might have been caused by the objective function which prioritized low angle of attack present in this type of configurations. However, since only a small number of double flap configurations had been tested, for the next tests the $HMCR$ value was changed to 0.5 for the $flap_2$ and $slat$ variables. The $HMCR$ controls if a variable is based on the HM or completely random, and the lowering of its value to 0.5 means that it is more likely to randomly generate these values and from that testing a broader type of configurations. Another option would be to increase the size of the HM; however it would result in a significantly run time increase, which is not intended in these test runs but it will be applied in the final run.

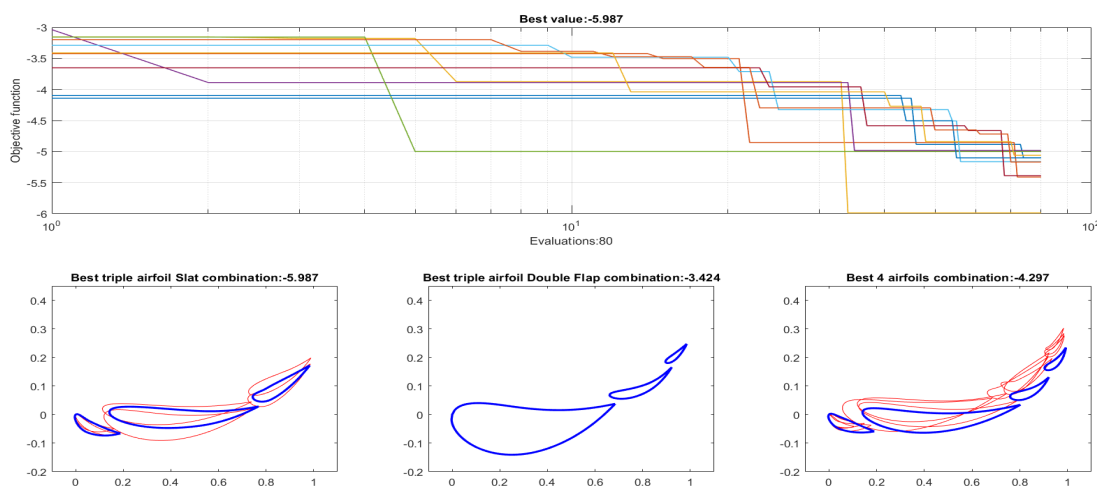
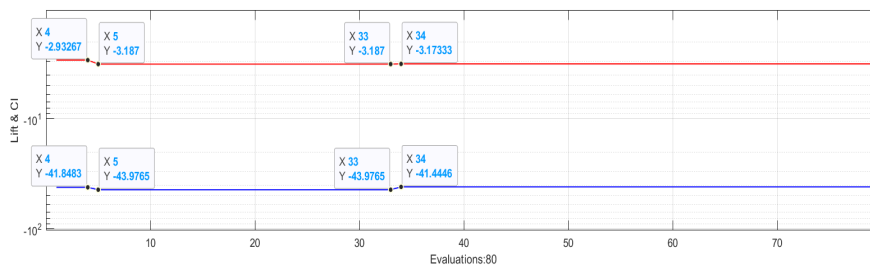


Figure 6.25: HM evolution and wing shapes with high levels of performance for each type of configuration for test run 1.

n_airfoils	f	alpha	CL	CL_Cd	L	D
3	-5.0991	10.4230	-3.2163	-10.7474	-42.1157	3.9187
3	-5.4101	8.9628	-3.3210	-11.6772	-41.5230	3.5559
3	-5.9866	9.8539	-3.1733	-14.4264	-41.4446	2.8728
3	-4.9830	9.8479	-3.2453	-10.1958	-42.9601	4.2135
3	-4.9994	11.2882	-3.1870	-10.4366	-43.9765	4.2137
3	-5.1621	10.6976	-3.2010	-11.0455	-41.3970	3.7478
3	-5.3880	10.3239	-3.2400	-11.8320	-41.0137	3.4663
3	-5.1013	9.3040	-3.6403	-9.4842	-45.6533	4.8136
3	-5.1681	9.6760	-3.3193	-10.7144	-41.6395	3.8863
3	-5.0589	10.1891	-3.6860	-9.1775	-47.5547	5.1816

Figure 6.26: HM values at the end of the first test run.

Figure 6.27: Lift and C_l best values during the evaluation process.

6.4.2 Test run with $S_1 = Lift$

Based on the conclusions withdrawn from the first test run, a new objective function $P = \beta S_1 + (1 - \beta)rS_2$, with $S_1 = Lift$, $S_2 = \frac{C_l}{C_d}$, $\beta = 0.75$ and $r = 4$ was tested together with the new $HMCR$ values. The whole optimization test run took 49 hours and had an average evaluation time of 33 minutes, the results evolution and final HM composition being found in Figures 6.28 and 6.29.

From these results, 3 main conclusions were withdrawn:

- From both figures it was possible to confirm that a wider variety of configurations was tested and can be found in the final HM; therefore, the $HMCR$ change will be kept for the next runs.
- From Figure 6.29 it is possible to confirm that the new optimization function is more appropriate for what is intended in this problem, since it is prioritizing the highly negative lift values.
- After the change in the objective function it was also possible to conclude that the value of $r = 4$ is not suitable anymore and should be changed to $r = 20$ since the values of $Lift(L)$ are about 20 times greater than the $\frac{C_l}{C_d}$ values, observed in Figure 6.29

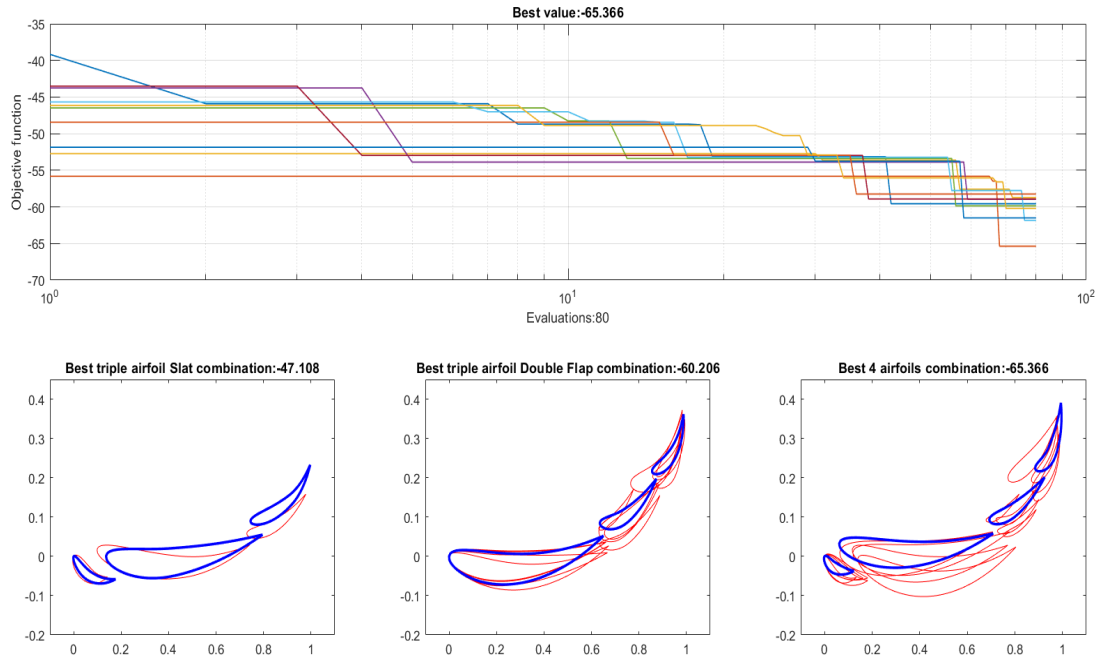


Figure 6.28: HM evolution and wing shapes with high levels of performance for each type of configuration for test run 2.

n_airfoils	f	alpha	CL	CL_Cd	L	D
3	-59.5668	17.4793	-3.3910	-3.3223	-74.9926	22.5722
4	-65.3658	19.7843	-3.5340	-3.9122	-81.9381	20.9444
3	-58.7159	17.8686	-3.1740	-4.4225	-72.3912	16.3690
4	-58.9630	20.9788	-3.2887	-3.7818	-73.5749	19.4549
3	-59.8546	20.7440	-3.2727	-3.0536	-75.7347	24.8016
4	-61.8481	20.0106	-3.4120	-4.0624	-77.0475	18.9661
4	-58.9160	16.2410	-3.4377	-4.4405	-72.6341	16.3573
4	-61.5018	17.6860	-3.4700	-4.1421	-76.4795	18.4638
3	-58.2424	18.7422	-3.1743	-3.3787	-73.1516	21.6505
3	-60.2056	19.8466	-3.2980	-3.3237	-75.8426	22.8187

Figure 6.29: HM values at the end of the second test run.

6.4.3 Test run with low quality mesh

Based on the conclusions withdrawn from the second test run, and due to the high run times, a run with a smaller mesh quality and faster evaluation times was tested. This test run wants to check if a lower quality simulation with deviated results could still achieve the same conclusions as an high quality simulation. The simulation was executed with the same configurations as in the previous test, keeping $r = 4$ to allow a fair comparison. In order to make that comparison, at the end of the run the best harmony inside the final HM was tested with an higher quality mesh and the results compared with the Section 6.4.2 results. The whole optimization test run took 15 hours and had an average evaluation time of 11 minutes, the results evolution and final HM composition being found in Figures 6.30 and 6.31.

From these results, 2 main conclusions were withdrawn:

- Discordant values, present in Figure 6.30, appeared due to the lack of mesh quality and normally associated with the slat proximity to the main wing, possibly compromising the optimization quality.
- From Figure 6.31 it was possible to conclude that the best feasible harmony is the one highlighted in blue, since the ones that presented a better objective function value also revealed non feasible C_l or C_d values. The C_l and C_d values, for the harmony represented in blue, obtained through the high quality simulation were close to the ones presented in the low quality mesh HM, less than 10% deviation. The high quality run executed in Section 6.4.2 revealed an overall better and more trustworthy performance. Nevertheless, lowering the mesh quality can be a viable option; however, it would demand another level of testing to viably understand how to evaluate the outsider values, either neglecting them or stopping them from affecting the optimization process.

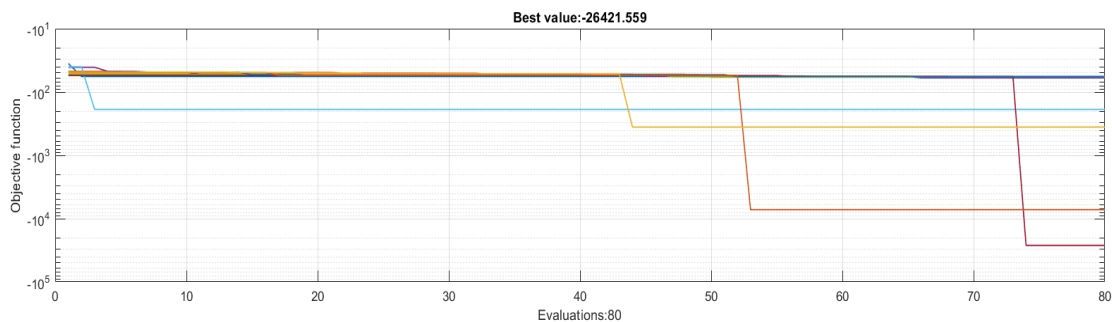


Figure 6.30: HM evolution and wing shapes with high levels of performance for each type of configuration for test run 3.

That said, with more understanding on the low quality mesh run an adaptive mesh run would be the ideal solution for this problem. The adaptive mesh run would start with a low quality mesh for the first iterations and the growth in mesh quality would coincide with the optimum value proximity, for this to happen the objective function values would have to be normalized and updated every time a new mesh quality was

introduced. For that more test runs would be needed to gain gain sensitivity on the subject and to correctly implement this optimal approach.

n_airfoils	f	alpha	CL	CL_Cd	L	D	frontal_area
4	-56.8314	20.5880	-3.0967	-3.7237	-69.5690	18.6825	0.1898
3	-59.2905	19.1178	-3.2080	-3.2886	-73.5730	22.3723	0.1938
3	-58.2686	19.9821	-3.1193	-3.7688	-71.4102	18.9476	0.1934
3	-59.9489	20.3417	-3.5660	-0.3609	-79.3304	219.8173	0.1880
3	-57.3053	20.1830	-3.1087	-3.3427	-70.8360	21.1916	0.1926
3	-188.6519	12.0078	-4.6230	-110.0714	-68.0835	0.6185	0.1919
4	-2.6422e+04	16.4628	-1.8190e+03	2.3100	-3.5233e+04	-1.5252e+04	0.1919
3	-56.9272	18.9084	-3.0770	-3.7060	-69.7262	18.8142	0.1915
3	-7.2253e+03	19.3214	-446.4383	0.6536	-9.6348e+03	-1.4742e+04	0.1824
3	-357.7265	16.3549	-24.6367	0.6777	-478.0982	-705.4714	0.1640

Figure 6.31: HM values at the end of the third test run.

6.4.4 Test run for one rear wing combination type

Based on the conclusions withdrawn from the third test run, the high quality mesh was used for this test. The test run wants to compare the joint optimization of three different types of configurations to the optimization of a single rear wing configuration type, and was done to check if the joint optimization of multiple types of configurations could have a negative effect on the optimization results. The test run was executed with the same configurations as in Section 6.4.2, keeping $r = 4$ to allow a fair comparison. The whole optimization test run took 48 hours and had an average evaluation time of 32 minutes, the results evolution and final HM composition being found in Figures 6.32 and 6.33.

From these results, a main conclusion was withdrawn:

- The results in Figure 6.33 were worse than the ones presented for a 4 airfoil type configuration on the HM of Section 6.4.2. Since a single wing type configuration optimization would result on a greater run time, since the process had to be replicated for all the three types and this approach didn't reveal any significant advantages, the joint optimization approach will be taken as default for the final run.

6.5 Final results

Based on the conclusions withdrawn from all the test runs, the final run was executed with the same configurations as in Section 6.4.2, with the exception of $r = 7.5$, the number of harmonies in the HM which was set to 20, and the maximum number of iterations changed to 400. The variable r , which is the member responsible for the magnitude equalization of both objective functions was initially set to $r = 20$ from the

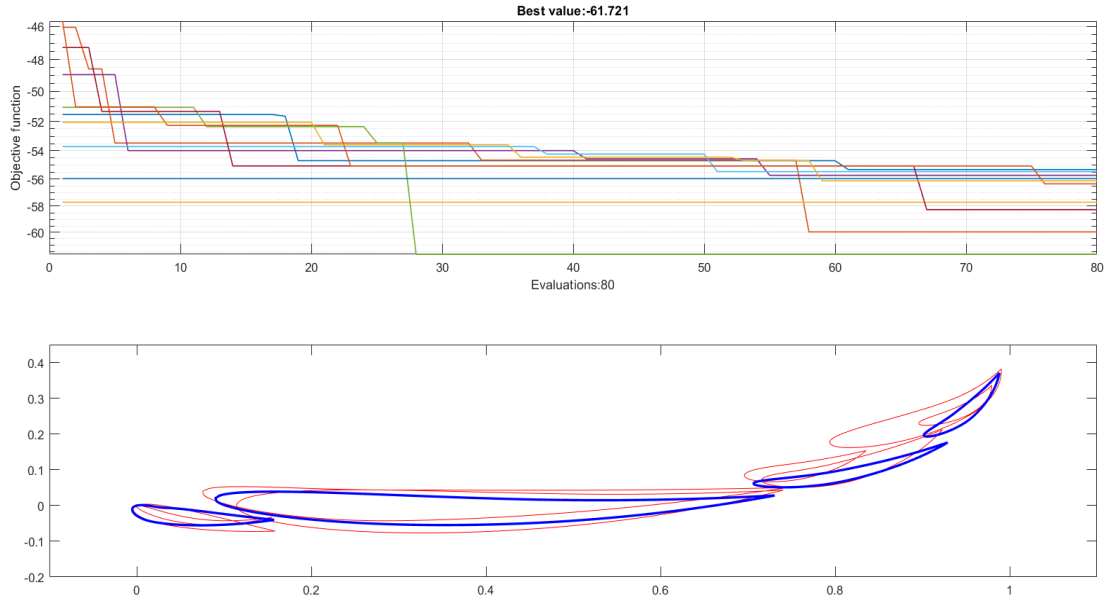


Figure 6.32: HM evolution and wing shapes with high levels of performance for each type of configuration for test run 4.

n_airfoils	f	alpha	CL	CL_Cd	L	D	frontal_area
4	-55.3262	19.7377	-3.2070	-3.8615	-68.6196	17.7701	0.1808
4	-59.9644	20.8588	-3.3433	-3.9387	-74.7008	18.9657	0.1888
4	-57.7118	21.0453	-3.1483	-3.0973	-72.8193	23.5103	0.1954
4	-55.7393	18.8242	-3.1743	-4.8198	-67.8927	14.0861	0.1807
4	-61.7210	20.5459	-3.4260	-3.6342	-77.4490	21.3109	0.1910
4	-55.4766	18.7807	-3.2520	-4.3412	-68.1805	15.7054	0.1772
4	-58.2656	20.4753	-3.2190	-3.5531	-72.9499	20.5313	0.1915
4	-55.9791	18.9228	-3.1443	-4.3332	-68.8612	15.8914	0.1851
4	-56.3576	17.4640	-3.4177	-4.1984	-69.5456	16.5646	0.1720
4	-56.1364	19.3589	-3.2307	-3.9787	-69.5437	17.4792	0.1819

Figure 6.33: HM values at the end of the fourth test run.

conclusions taken in the test runs; however, since $\frac{C_l}{C_d}$ could reach values close to 10 in certain rear wing configurations, $r = 20$ would result in a prioritization of the $\frac{C_l}{C_d}$ over the Lift values, which is not intended. With further testing the value $r = 7.5$ revealed to be the best value for this problem. The whole optimization test run took 230 hours (1 week 2 days 14 hours) and had an average evaluation time of 33 minutes, the results evolution and final HM composition being found in Figures 6.34 and 6.35.

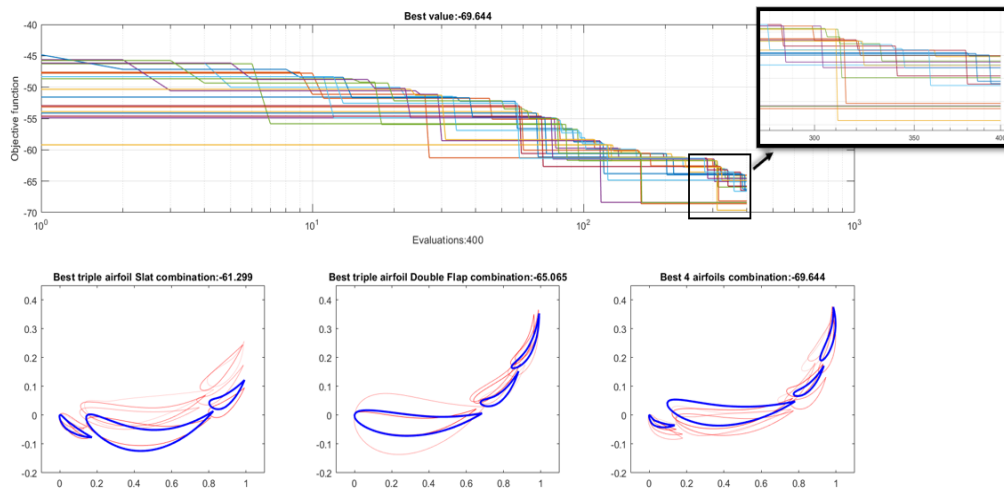


Figure 6.34: HM evolution and wing shapes with high levels of performance for each type of configuration for the final run.

The 4 airfoil type configuration was the best performing rear wing configuration, confirming that the addition of a small sized slat to the two flaps could be beneficial. From the final run resulted the wing configuration present in Figure 6.34, whose performance values can be found highlighted in blue in Figure 6.35. The full rear wing is able to produce 166 N of downforce while only producing 42 N of Drag force. When compared to the values produced by the rear wing of the winning team of the 2016 Czech Republic FSAE event winners, in Iljaž et al. (2016)[5], revealed an reduction of 35% of Drag force while producing the same amount of downforce. The aerodynamic performance values for the rear wing found in that article were also obtained for 50 km/h and simulated with the car. Unfortunately no values of the isolated rear wing performance were found for more recent winning teams.

It is also important to add that the rear wing found in Iljaž et al.(2016) [5] uses a gurney flap on the last flap of its configuration, and an optimized end-plate which improves its performance, while the generated optimized wing in this thesis could still be improved by that type of devices. The car in that article also has a lower driving position, which allows for more undisturbed flow to reach the rear wing, and has a front wing designed to redirect the air stream to the rear wing which again improved the obtained results. Finally, the final run had to be set to 400 iterations due to the time it took; however, from Figure 6.34 it is possible to conclude that the optimization has not completely converged, and could be given a bigger number of iterations to reach an even more optimized configuration.

n_airfoils	f	alpha	CL	CL_Cd	L	D	frontal_area
4	-64.0551	18.1415	-3.5700	-4.1838	-74.9474	17.9139	0.1774
4	-68.6080	17.5998	-3.6263	-3.6600	-82.3273	22.4938	0.1918
4	-64.1230	20.9130	-3.3670	-4.0668	-75.3305	18.5235	0.1891
3	-65.0651	19.5919	-3.4700	-3.4339	-78.1686	22.7635	0.1904
4	-64.4970	20.5066	-3.3613	-3.5962	-77.0056	21.4133	0.1936
4	-65.0940	15.4863	-3.6160	-3.6115	-77.7631	21.5318	0.1817
4	-65.7837	18.7228	-3.4597	-3.8551	-78.0739	20.2523	0.1907
4	-66.2389	19.9827	-3.5430	-4.2122	-77.7881	18.4674	0.1855
4	-64.0237	18.8228	-3.3400	-4.6904	-73.6391	15.7001	0.1863
4	-69.6436	17.5640	-3.7483	-3.9311	-83.0303	21.1212	0.1872
4	-68.3763	15.2248	-3.6563	-3.7866	-81.7020	21.5766	0.1888
4	-65.9415	19.4206	-3.5090	-3.7122	-78.6415	21.1847	0.1894
3	-64.8429	19.1006	-3.3683	-3.3374	-78.1137	23.4055	0.1960
4	-66.4874	18.9539	-3.4310	-4.1757	-78.2107	18.7301	0.1926
4	-66.4481	17.7057	-3.5320	-3.6280	-79.5274	21.9203	0.1903
4	-68.1608	19.0110	-3.6110	-3.4674	-82.2124	23.7098	0.1924
4	-64.8742	20.7200	-3.3303	-3.9900	-76.5239	19.1789	0.1942
4	-64.5853	19.6983	-3.3047	-3.7947	-76.6270	20.1932	0.1959
4	-68.4120	18.0989	-3.6320	-3.4085	-82.6947	24.2612	0.1924
4	-66.6110	17.0755	-3.5367	-3.5505	-79.9383	22.5146	0.1910

Figure 6.35: HM values at the end of the final run.

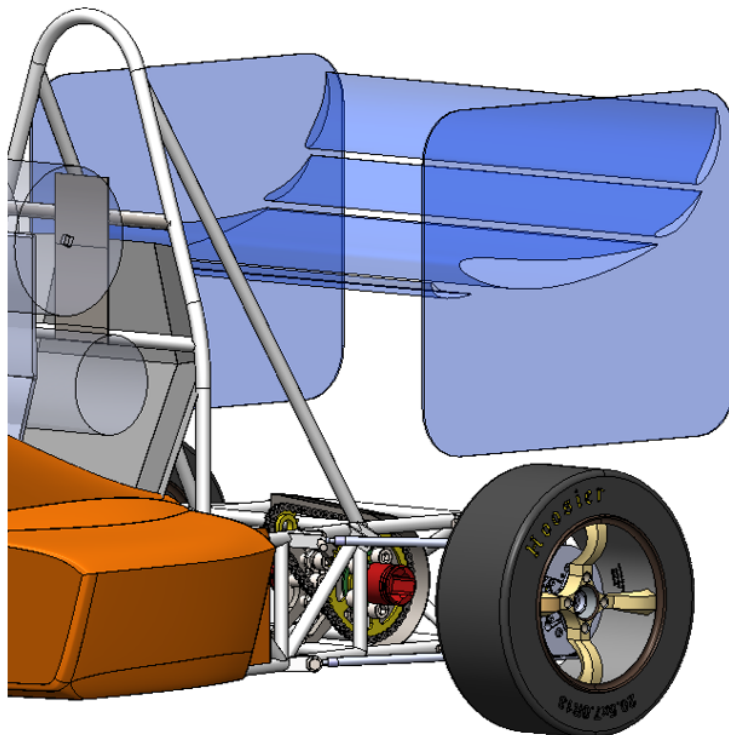


Figure 6.36: Optimized rear wing.

Part III

Conclusions and suggestions for future work

Chapter 7

Conclusions and suggestions for future work

This work aimed and succeeded at developing a functional optimization code capable of delivering a personalized high performance rear wing geometry, providing geometries for any Formula Student type car through a velocity profile obtained by CFD analysis. In order to obtain the desired results and to work as a proof of concept, the UA Formula Student car was selected and its optimal rear wing obtained.

In the first part, after an analysis to both CFD theoretical background and to the default aerodynamic devices, the UA Formula Student car was the object of a set of CFD simulations, in which every parameter controlling the meshing and simulation setup was thoroughly evaluated and investigated. A stable and accurate simulation was set through mesh independence studies and boundary layer refinements.

Additionally, wind tunnel experiments were conducted for a 3D printed 1/4 scale model of the Formula Student vehicle, being the flow measurements carried out using the PIV technique, which was able to provide a velocity vector field to be compared with the simulation results, where once more the quality of the CFD simulations, for low velocities and no wheel rotation, was confirmed by the similarity of both velocity fields. For this section, further improvements can be made in future work, being some of them increasing wind tunnel flow velocity while adding rotating wheels to the wind tunnel experiments, and even producing a scaled transparent side-pod in order to enable a better flow visualization.

Hereupon, the challenge of creating a functional rear wing optimizer was surpassed, starting by developing scripts to automate all the optimization process and to communicate between two different software. Combining these with the HSA, which was adapted for the problem at hands, and after a great number of runs to debug all the process, a set of test runs was executed for a better understanding of what would be the optimal problem approach. Once found the optimal parameters that control the optimization algorithm, a final run was executed. The final solution showed significant improvements over the 2016 Czech Republic FSAE winning car, reaching the same values of downforce for a drag reduction of 35%, despite the obvious advantages in terms of driver seating position and extra aerodynamic devices as the gurney flap and more optimized end-plates.

The rear wing optimization could also be expanded to new horizons by introducing

a new level of flexibility to the airfoils shape by using B-splines or Bézier surface parameterization which enable more innovative airfoil shapes. A multi point objective optimization would also be beneficial for future improvements, since it would allow the optimization of the rear wing to be conducted for various flow velocities and even different car conditions, both in a straight line and while curving.

Finally, as a last suggestion for future work, the optimization code could be adapted to develop curved wings, where the variation in the airfoil section would be defined by splines and the airfoil shape could be maintained constant or even changed over the wing length, like the ones currently used by some of the best formula student teams.

In brief, the goals of this work have been fulfilled, and both the carried out CFD analysis and the developed rear wing optimization code will enhance the knowledge of future team members, leading to a faster, more performant and better designed Formula Student vehicle.

Bibliography

- [1] D. Case. *Formula SAE: Competition History 1981-2004*. Society of Automotive Engineers, 2005.
- [2] Formula Student Germany. *Formula Student Rules 2021*. July 2020. URL: <https://www.formulastudent.de/fsg/rules/>.
- [3] M. Chen, W. Tang, and B. Yang. "Computer-aided front and rear wings aerodynamic design of a formula SAE racing car". In: *Applied Mechanics and Materials*, vol 81, (2012), pp. 20–25.
- [4] I. Oxyzoglou. "Design Development of an Aerodynamic Package for an FSAE Race Car". MSc Thesis. University of Thessaly, Dep. of Mechanical Engineering, 2019.
- [5] J. Iljaž, L. Škerget, and M. Štrakl. "Optimization of SAE formula rear wing". In: *Strojniski Vestnik/Journal of Mechanical Engineering*, vol 62, (2016), pp. 263–272.
- [6] S. Leblanc. *Analysis of the Effects of Slot Gaps on Multi-Element Wings*. Tech. rep. Austin: The University of Texas, Dep. of Aerospace Engineering and Engineering Mechanics, 2016.
- [7] H. Dahlberg. "Aerodynamic development of Formula Student race car". In: (2014). URL: <http://www.diva-portal.org/smash/record.jsf?pid=diva2:737287>.
- [8] S. McBeath. *Competition Car Aerodynamics A Practical Handbook*. 3rd ed. England: Veloce Publishing, 2015.
- [9] C. Fu, M. Uddin, and C. Zhang. "Computational analyses of the effects of Wind tunnel ground simulation and blockage ratio on the aerodynamic prediction of flow over a passenger vehicle". In: *Vehicles*, vol 2, (2020), pp. 318–341.
- [10] W. H. Hucho. *Aerodynamik des Automobils: Strömungsmechanik, Wärmetechnik, Fahrdynamik, Komfort*. Vieweg + Teubner Verlag, 2013.
- [11] R. K. Hanna. "CFD in sport - A retrospective; 1992 - 2012". In: *Procedia Engineering*, vol 34, (2012), pp. 622–627.
- [12] J.D. Anderson. *Fundamentals of Aerodynamics*. 5th ed., Maryland, 2013.
- [13] J.H. Ferziger/M. Perić. *Computational Methods for Fluid Dynamics*. 3rd ed. Germany: Springer-Verlag, 2002.
- [14] J.D. Anderson. *Computational Fluid Dynamics: The Basics with Applications*. USA: Maryland, 1995.
- [15] S. P. Neill and M. R. Hashemi. "Ocean Modelling for Resource Characterization". In: *Fundamentals of ocean renewable energy*. 2018, pp. 193–235.

- [16] J. Tan. "Study of Solving Navier-Stokes Equations with a Finite Volume Method based on Polygonal Unstructured Grids and the Computational Analysis of Ground Vehicle Aerodynamics". MSc Thesis. Texas Tech University, Dep. of Mechanical Engineering, 2010.
- [17] ANSYS Inc. "ANSYS Fluent Theory Guide". In: *ANSYS Inc., USA* January (2021).
- [18] J. O. Hinze. *Turbulence*. New York: McGraw-Hill Publishing Co, 1975.
- [19] M. S. Ferreira. "Multidisciplinary Design Analysis and Optimisation of Rear Wings for Sports Cars". MSc Thesis. Instituto Superior Técnico, Dep. of Aerospace Engineering, 2016.
- [20] F. Mariani, C. Poggiani, and F. Risi. "Formula-SAE racing car: Experimental and numerical analysis of the external aerodynamics." In: *Energy Procedia* , vol 83, (2015), pp. 1013–1029.
- [21] ANSYS Inc. "ANSYS FLUENT User's Guide". In: *ANSYS Inc., USA* January (2021).
- [22] ANSYS.Inc. *White Paper ANSYS Fluent Mosaic Technology*. 2018.
- [23] W. H. Hucho and G. Sovran. *Aerodynamics of Road Vehicles: From Fluid Mechanics to Vehicle Engineering*. Ed. by Wolf-Heinrich Hucho. Cambridge, 1993.
- [24] L. P. Correia, S. Rafael, and V. Rodrigues. "High-resolution analysis of wind flow behavior on ship stacks configuration: A Portuguese case study". In: *Atmosphere* , vol 12, (2021), pp. 1–17.
- [25] Joseph Katz. *Race Car Aerodynamics : Designing for Speed*. Cambridge: Bentley Publishers, 2006.
- [26] F.M. White. *Fluid Mechanics*. 2nd ed. ,New York, NY, USA, McGraw-Hill, 1986.
- [27] S. Diasinos. "The Aerodynamic Interaction of a Rotating Wheel and a Downforce Producing Wing in Ground Effect". MSc Thesis. University of New South Wales, Dep. of Mechanical Engineering, 2009.
- [28] Frystak L. "Formula SAE Aerodynamic Optimization". MSc Thesis. Brno University of Technology, Dep. of Mechanical Engineering, 2016.
- [29] L. Abreu. "Mechanical Design of the Wheel Assembly of an Electric Formula Student Prototype". MSc Thesis. Instituto Superior Técnico, Dep. of Mechanical Engineering, 2019.
- [30] Frankie F. J. *Aerodynamic optimisation of Formula student vehicle using computational fluid dynamics*. 2018.
- [31] P. Novais and J. Sarmento. "Otimização de problemas com recurso ao Harmony Algorithm ". In: *A. G. Campos, J. D. Oliveira. Coordinators, Otimização Não-Linear em Engenharia – Trabalhos e Aplicações 2020/2021* (2021). doi: <https://doi.org/10.48528/46r9-gv78>.
- [32] A. Askarzadeh and E. Rashedi. "Harmony Search Algorithm: Basic Concepts and Engineering Applications". PhD thesis. University of Advanced Technology, Iran, 2017.
- [33] M. Mahdavi, M. Fesanghary, and E. Damangir. "An improved harmony search algorithm for solving optimization problems". In: *Applied Mathematics and Computation* , vol 188, (2007), pp. 1567–1579.